ACS NANO

Cite This: ACS Nano 2018, 12, 7771−7790

www.acsnano.org

ARTICLE

Age-Dependent Rat Lung Deposition Patterns of Inhaled 20 Nanometer Gold Nanoparticles and their Quantitative Biokinetics in Adult Rats

Wolfgang G. Kreyling,*[,‡,§] Winfried Möller,[‡,†] Uwe Holzwarth,[∥] Stephanie Hirn,[‡] Alexander Wenk,[‡,#] Carsten Schleh,[‡,▽] Martin Schäffler,[‡] Nadine Haberl,[‡] Neil Gibson,[∥] and Johannes C. Schittny[⊥]

[‡]Comprehensive Pneumology Center, Institute of Lung Biology and Disease, Helmholtz Zentrum München—German Research Center for Environmental Health, Ingolstaedter Landstrasse 1, D-85764 Neuherberg/Munich, Germany

[§]Institute of Epidemiology, Helmholtz Center Munich—German Research Center for Environmental Health, Ingolstaedter Landstrasse 1, D-85764 Neuherberg/Munich, Germany

[∥]Directorate for Health, Consumers and Reference Materials, Joint Research Centre, European Commission, Via E. Fermi 2749, I-21027 Ispra, Varese, Italy

[⊥]Institute of Anatomy, University of Bern, Baltzerstrasse 2, CH-3012 Berne, Switzerland

Supporting Information

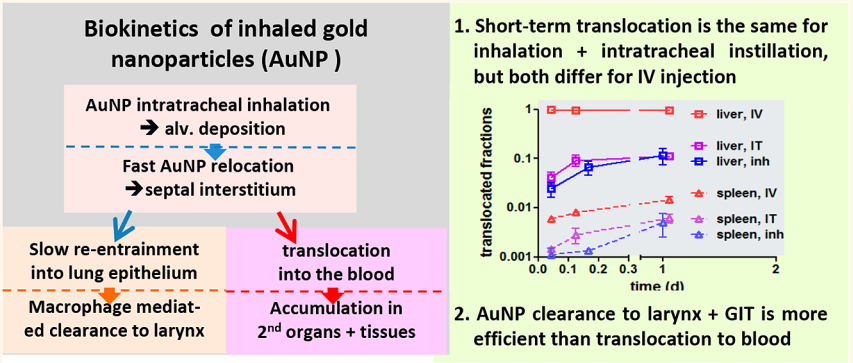

ABSTRACT: The increasing use of gold nanoparticles leads to a possible increase of exposure by inhalation. Therefore, we have studied the deposition patterns of inhaled 20 nm gold nanoparticles (AuNP) in 7−90 day old rats and their biokinetics in 60 day old ones. Wistar−Kyoto rats inhaled intratracheally 20 nm ^{195}Au-radiolabeled AuNP by negative pressure ventilation over 2 h. Immediately afterward lungs were excised, inflated and microwave dried. AuNP deposition was analyzed by single-photon emission computed tomography, computed-tomography and autoradiography. Completely balanced, quantitative biodistributions in major organs and all body tissues and total excretion were analyzed from 1 h to 28 d after inhalation. Intratracheal inhalation caused AuNP deposition predominately in the caudal lungs, independent of age. About 30% AuNP were deposited on airway epithelia and rapidly cleared by mucociliary clearance. About 80% of AuNP deposited in alveoli was relocated from the epithelium into the interstitium within 24 h and was inaccessible to broncho-alveolar lavage. During interstitial long-term retention, re-entrainment within macrophages back onto the lung epithelium and to the larynx and gastrointestinal tract (GIT) dominated AuNP clearance (rate 0.03 d^{-1}) In contrast, AuNP-translocation across the air−blood barrier was much smaller leading to persistent retention in secondary organs and tissues in the ranking order liver > soft issue > spleen > kidneys > skeleton > blood > uterus > heart > brain. The age-independent, inhomogeneous AuNP deposition was probably caused by the negative pressure ventilation. Long-term AuNP clearance was dominated by macrophage-mediated transport from the interstitium to the larynx and GIT. Translocation across the rat air−blood barrier appeared to be similar to that of humans for similar sized AuNP.

continued...

Received: March 10, 2018
Accepted: August 7, 2018
Published: August 7, 2018

DOI: 10.1021/acsnano.8b01826
ACS Nano 2018, 12, 7771−7790

KEYWORDS: *gold nanoparticle aerosols, intratracheal inhalation, air−blood barrier translocation, extrapulmonary nanoparticle accumulation, nanoparticle clearance, alveolar macrophage, interstitial nanoparticle relocation, epithelial re-entrainment*

Gold nanostructures and especially gold nanoparticles (AuNP) hold great promise as catalysts. They make the industrial production of many plastic materials "greener" by reducing energy consumption, reducing undesired byproducts, and replacing environmentally problematic catalyst materials.[1] Furthermore, gold nanostructures offer milder reaction conditions and a higher selectivity that may be advantageous in pharmaceutical production.[2] Therefore, an increasing use of AuNP in industrial processes is anticipated,[1,3,4] leading to increased professional and possibly environmental exposure. As a result, numerous noninhalation based studies on the toxicity and biodistribution of AuNP have been reported which have been reviewed in refs 5−7. Recently, the use of inhaled AuNP as drug carriers[8] and as radiosensitizers[9] has been proposed for the treatment of lung cancer, where inhalation is expected to allow a more specific and direct access to diseased tissue, reducing risks associated with systemic application. Unintentional exposure to AuNP aerosols and intentional inhalation for therapeutic purposes means that sufficient knowledge should be obtained about AuNP deposition and retention in the lungs and about their biokinetics fate and accumulation in secondary organs and tissues of the entire organism.

Only two inhalation studies on truly nanosized AuNP in experimental animals have been reported[10,11] (besides our papers[23−26]), and very recently, a new review appeared on the biokinetics of inhaled nanomaterials.[12] In both aforementioned studies, the AuNP consisted of agglomerates of smaller primary gold particles in contrast to the heat-treated AuNP used in our study. Furthermore, very recently, a human inhalation study appeared using AuNP similarly generated and sized as those of our study which mainly focused on the AuNP toxicity with some information on deposition and biokinetics.[13]

Recently, we have studied the fate of inhaled, ^{192}Ir-radiolabeled, 20 nm iridium nanoparticles [^{192}Ir]IrNP in the same strain of rats as used in the present study.[14−16] We observed that these [^{192}Ir]IrNP were relocated rapidly from the alveolar epithelium into the epithelial and septal interstitial spaces. This finding was strikingly different to the behavior of inhaled 1.3 μm sized fused alumino-silica particles[17] and intratracheally instilled 2.1 μm sized polystyrene particles[18] in rodents. These micrometer-sized particles did not relocate from the epithelial surface but were retained in alveolar macrophages (AM) on the epithelial surface. From there, they were gradually transported to the larynx and were swallowed into the gastro-intestinal tract (GIT). This clearance process resulted in a half-life of 60−70 days for the microparticles in the lung. Surprisingly, a major fraction of the [^{192}Ir]IrNP were not retained on the epithelium but rapidly relocated into the interstitium. From there, they were slowly re-entrained back onto the lung epithelium and predominantly cleared via the ciliated airways up to the larynx and swallowed into the GIT. It can be noted that from day 1 after inhalation during long-term retention, more than 90% of [^{192}Ir]IrNP recovered by broncho-alveolar lavage (BAL) was associated with macrophages. This means long-term re-entrainment was macrophage mediated. The fractional clearance rates via the GIT and the determined clearance half-life were rather similar to the 60−70 days as observed for the micrometer-sized particles. Hence, for the present study, we hypothesized that the peculiar [^{192}Ir]-IrNP long-term lung-internal NP transport phenomena may be the same for AuNP of the same size. This hypothesis would indicate that an intermediate interstitial storage and release of nanoparticles back onto the lung epithelium may be a NP-specific phenomenon.

RESULTS AND DISCUSSION

Rationale and Aims. The present study was designed to investigate (a) the age-dependent pulmonary deposition of AuNP and (b) the quantitative biokinetics of AuNP over 28 days after a single 2 h intratracheal inhalation of ^{195}Au radiolabeled 20 nm AuNP ([^{195}Au]AuNP) freshly generated by aerosol spark ignition. The biokinetics fate of the AuNP was studied only in adult rats (8−10 weeks old female rats[14−16]). However, we hypothesized that the age dependency of 20 nm [^{192}Ir]IrNP deposition[19] holds also for 20 nm sized AuNP, and therefore we investigated the deposition patterns in different-aged rats ranging from newborn to adulthood in the present study. In addition, using 3D-imaging, we aimed to test the hypothesized homogeneous [^{195}Au]AuNP deposition in the lungs of differently aged rats, which is governed by diffusional NP transport in the lung air spaces during breathing. Deviating from earlier age-dependent [^{192}Ir]IrNP deposition studies, where the rats were exposed via spontaneous breathing in a nose-only inhalation apparatus, in the present study, the rats were ventilated in a low-pressure plethysmograph box via an endotracheal catheter, which allowed a much more controlled inhalation exposure. Additionally, collateral skin contamination was essentially avoided (which might have hampered the quality of the subsequent quantitative biokinetics studies). We are aware that intratracheal inhalation may have affected deposition and distribution of the inhaled aerosol. Specifically, the artificial ventilation may have affected both chest wall and diaphragm movement during breathing, eventually resulting in changes of NP deposition in the upper *versus* the lower lung of different-aged rats. In the present study, the AuNP were radiolabeled with ^{195}Au instead of ^{198}Au in order to benefit from a longer radioactive half-life of 186 days instead of only 2.7 days in previous studies. Furthermore, for the biokinetics, we focused on one size of inhaled NP (20 nm), while in previous studies we applied monodisperse [^{198}Au]AuNP of different sizes (1.4, 2.8, 5, 18, 80, and 200 nm) either by intratracheal (IT) instillation,[20] by intraesophageal instillation (gavage)[21] or by IV injection.[22] In the latter experiments the short half-life of ^{198}Au restricted the follow-up of the biokinetics to 24 h. We hypothesized that the biokinetics of **intratracheal-instilled** 18 nm [^{198}Au]AuNP may distinctly differ from that of **inhaled** 20 nm [^{195}Au]AuNP due to patchier and less deep AuNP deposition in the alveolar region. Additionally, a comparison of the present results with the earlier experiments during the first 24 h post exposure (p.e.) allow a direct evaluation as to whether the biokinetics of same sized AuNP in rats of same age and strain applied by IV injection is a suitable approach to predict that of either inhaled or IT-instilled AuNP.

DOI: 10.1021/acsnano.8b01826
ACS Nano 2018, 12, 7771−7790

The biokinetics part of the present study was also designed to compare the biokinetics of two different inhaled 20 nm NP materials, AuNP and IrNP,[14−16] including their translocation kinetics across the air−blood barrier (ABB) and their accumulation in secondary organs and tissues in the same strain of rats using the same inhalation technology. In addition, it should be noted that there are no biokinetics studies available for inhaled 20 nm sized NP because other inhalation studies applied larger sized agglomerates of NP.

Another aspect of the current study deals with the possible relocation of 20 nm [^{195}Au]AuNP into the alveolar interstitium and subsequent re-entrainment back onto the lung epithelial surface as previously observed for 20 nm [^{192}Ir]IrNP.

Retained NP crossing the lung-ABB into circulation will interact and eventually are phagocytized by cells of the mononucleated phagocyte systems (MPS; e.g. macrophages, neutrophils, monocytes) existing in most organs (e.g., liver, spleen, kidneys), in bone marrow of the skeleton, and in other tissues (e.g., connective tissue, muscle). Hence, NP will be cleared from blood. However, as reviewed by Hume,[23] the locations of MPS cells, their status of differentiation, and their surface markers differ between organs. Hence, the rates of phagocytosis depend not only on NP properties like size, shape, and surface parameters but also on MPS functions. As a result, distribution, retention, and clearance of NP in these organs are complex and are not yet fully understood.[24−27] Comparing the present results with our previous studies after intratracheal instillation, oral gavage, or intravenous injection (IV) of 20 nm AuNP,[20−22] we will discuss the role of MPS in different organs.

Because of the design of the present study, we could not focus on the AuNP distribution at a microscopic level. However, by applying the same AuNP generation technology by spark ignition and similar inhalation methods, we have studied the microscopic fate of similar sized (20 nm) retained AuNP in the lungs of rats[28,29] and mice[30,31] by transmission electron microscopy (TEM) and by mass-based analyses, mainly immediately after inhalation and during the first 24 h. In both species, AuNP were found on the lung epithelium either as free luminal AuNP (mostly directly p.e.), as well as in AM and alveolar epithelial type I cells (EC1), preferentially after several hours. Much smaller numbers of AuNP were found in vascular endothelia. Most intracellular AuNP were retained in vesicles of both cell types. Initially, individual and small agglomerates of AuNP were observed in the cells but with increasingly time larger AuNP agglomerates were observed, indicating agglomeration inside the cells.

Part 1: Age Dependent [^{195}Au]AuNP Deposition Distribution. Rats, ventilated in a low-pressure plethysmograph, were exposed to freshly generated 20 nm [^{195}Au]AuNP at postnatal days 7, 14, 21, 35, 60, and 90. The total deposition per lung increased due to the larger lung volume with increasing age (Table 1 and Figure S3 of Supporting Information). Additionally, the total deposition per lung volume showed a temporally inhomogeneous distribution (Figure 1). For the younger rats at age 7 d or 14 d, the [^{195}Au]AuNP content per lung volume was low. It reached its peak at an age of 21 days, where the deposition per lung volume was about three times higher than in the younger rats. With increasing age, it dropped again (Figure 1, Table 1). This finding is in good agreement with previous findings using 20 and 80 nm [^{192}Ir]IrNP and rats of the same strain, where a low pulmonary retention was observed at ages of 7 and 14 days, a very high retention at 21 days, and a medium one in older aged rats.[19]

The peak of [^{195}Au]AuNP content per lung volume at an age of 21 days may be explained by structural alterations taking place during postnatal rat lung development.[32] First, the mean volume of the alveolar airspaces decreases by a factor of ∼4 between days 4 and 21 and increases by a factor of ∼2 between days 21 and 36 or 60, respectively. [In rats on postnatal day 4, airspaces are still sacculi because the formation of the alveoli (alveolarization) did not yet start. To keep the text readable, we simplified this point.] It seems to be that small alveoli promote a higher rate of diffusional particle deposition. Second, the number of acini stays constant throughout postnatal lung development, but the acinar volume increases in rats by a factor of ∼20 between days 4 and 60.[33] *In silico* (computational fluid dynamics) studies of respiratory flows and acinar aerosol transport,[34] multiple-breath nitrogen washout,[35] and our own unpublished results (JCS) predict that particle deposition increases with increasing size of the acini. The latter may explain why the deposition per lung volume does not decrease as much as we would have expected based on the decrease of the mean alveolar volume after day 21.

Table 1. Parameters and Data Retrieved from the [^{195}Au]AuNP Aerosol Deposition Distribution Analysis Performed with Rats of Different Ages[a]

	age of rat (d)					
	7	14	21	35	60	90
body weight (g; BW)	14.2	30.3	37	134	255	308
total lung capacity (cm^3; TLC)[b]	1.03	1.79	1.69	4.67	6.77	8.01
tidal volume (cm^3)[b]	0.78	1.35	1.26	3.50	5.08	6.01
deposited ^{195}Au activity (kBq)[c]	4.93	7.75	23.88	51.08	58.67	91.38
deposited AuNP mass (μg)[b]	3.18	5.00	15.41	32.95	37.85	58.95
deposited AuNP mass/total lung capacity (μg/cm^3)	3.09	2.79	9.12	7.06	5.59	7.36

[a]Footnotes to the table: the deposition data were derived from γ-spectrometric analyses of the excised lungs. [b]Calculated according to Tschanz et al., 2014.[36] [c]According to eqs 4−14 of Supporting Information.

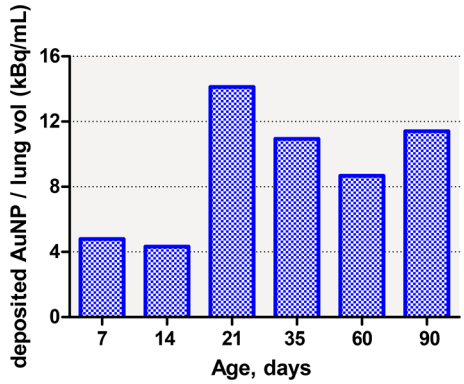

Figure 1. Deposited [^{195}Au]AuNP per lung volume. The concentration of deposited [^{195}Au]AuNP dose was calculated from the total deposited dose and the total lung volume.

DOI: 10.1021/acsnano.8b01826
ACS Nano 2018, 12, 7771−7790

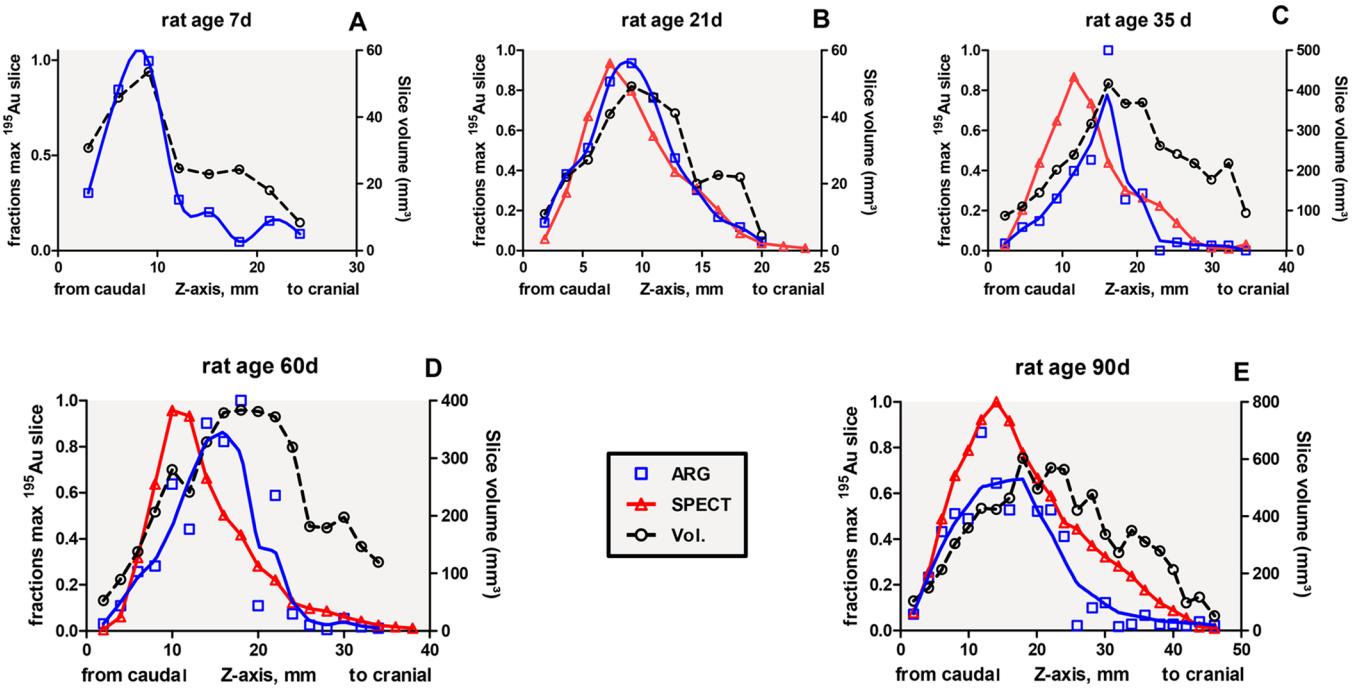

Figure 2. [^{195}Au]AuNP distribution in transversal slices of the right lung of the different aged rats analyzed by SPECT (red triangles and red solid lines) and by autoradiography (blue squares, blue solid lines) from caudal to cranial. The volumes of lung slices are calculated from the autoradiographic VOXEL volume of each slice (black circles, black dashed lines).

Besides the total deposited dose, the spatial distribution pattern of the deposited [^{195}Au]AuNP activity in the animals was derived from single photon emission computed tomography (SPECT) imaging of the excised lungs that were dried under fully inflated conditions. A 3−4-fold higher fraction of the [^{195}Au]AuNP aerosol was deposited in the caudal part of the lungs compared to the cranial part (Figure S3 of Supporting Information). This result was confirmed by autoradiography. Figure 2 shows the transversal slices data of the right lung from SPECT and autoradiography, indicating a good agreement between both methodologies. Additionally, the estimated volumes of the right lung slices used for autoradiography (as calculated from slice surface and thickness) are plotted by emphasizing that caudal lung volumes were more ventilated and received more [^{195}Au]AuNP deposition than cranial volumes.

The increased deposition in the caudal region of both lungs resulted most likely from the negative pressure ventilation of each rat lying on its left lateral side within the plethysmograph box. This breathing maneuver caused predominant diaphragmatic ventilation compared to chest wall ventilation, resulting in enhanced ventilation and [^{195}Au]AuNP deposition in the caudal lungs because of their higher compliance to the diaphragmatic movement. The predominant deposition in the caudal lungs was observed in rats of all ages.

Figure 3 shows qualitatively a higher deposition of the right *versus* the left lung for all ages. This effect was studied early on in human lung physiology at different exposure positions and was reviewed by Hughes and Amis.[37] In fact, at exposure on the left lateral side, gravity causes a larger expansion of the right lung alveoli (upper side) compared to the dependent left lung alveoli, resulting in higher deposition in the upper part of the lungs. Interestingly, two times higher deposition in the right lung compared to the dependent left lung is also predicted by the multiple-path particle dosimetry model (MPPD) in Table S1 (lower part) of Supporting Informaion when the rat is supported on its left lateral side.

Because diffusive (thermodynamic) deposition is by far the most important mechanism for the deposition of spherical particles below a diameter of 100 nm,[38] we may view particle deposition of our 20 nm particles as a measure for ventilation.

Figure 3 shows a series of 10 transversal slices of the total lungs of rats of 21 d, 35 d, 60 d, and 90 d age from caudal to cranial. The pinhole geometry of the SPECT images inverts the left lung to the right and vice versa. The slices of all rats show [^{195}Au]AuNP deposited in both lungs but also indicate slight left to right inhomogeneities. The [^{195}Au]AuNP deposition inhomogeneity from caudal to cranial is evidenced in both Figures 2 and 3.

Although age dependent deposition is only shown for one rat of each age, the trend of the results is confirmed by the following points: (a) total deposition dose increases with age due to the increasing lung volume and inhaled volume with age, (b) both the increasing total deposited dose and the higher deposition per lung volume at an age of 21 d (when compared to younger baby rats and older adult rats) is confirmed by four more rats of each age of the same rat strain in our previous inhalation studies using 20 nm sized [^{192}Ir]IrNP,[19] and (c) the unexpected inhomogeneity of deposition of the cranial region *versus* the caudal region is consistently confirmed by two independent methodologies SPECT gamma camera and autoradiographic analyses.

Part 2: Biokinetics Study of Adult Rats. Table 2 compiles all aerosol parameters for the 2 h intratracheal inhalation studies for each group of rats.

Intratracheal inhalation exposure led to intrathoracic airway deposition as well as alveolar deposition. The results show that alveolar retention is the dominating long-term effect. In Table 3, the parameters of aerosol inhalation and deposition are compiled for each group of rats used in the biokinetics study.

DOI: 10.1021/acsnano.8b01826
ACS Nano 2018, 12, 7771−7790

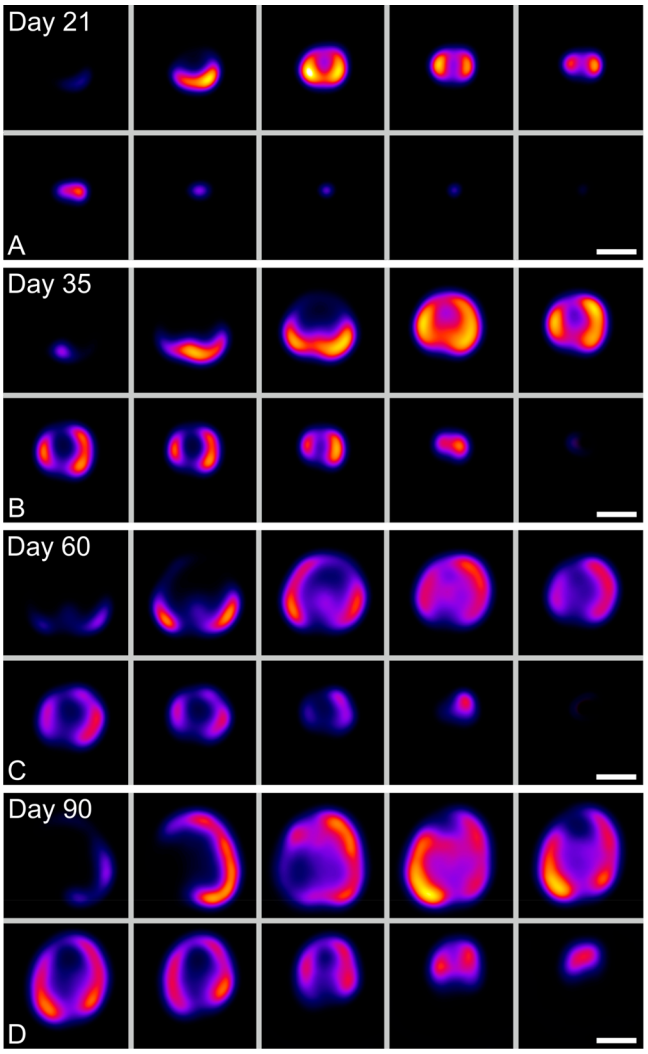

Figure 3. Series of transversal slices (perpendicular to spinal axis) of the total lungs of rats of 21 d, 35 d, 60 d, and 90 d age from caudal to cranial. Note the pinhole geometry of the SPECT images inverts left to right lung and vice versa. The thickness of the reconstructed slices was 1 mm; only every fourth slice is shown. The scale bar indicates 1 cm. Because of the small size of the lungs of the 7 d and 14 d rats, a 3D reconstruction was not possible under the pinhole geometry of the SPECT images.

In addition, the activity fractions cleared from the lungs that can be attributed to fast mucociliary clearance from the conducting airways (MCC) and long-term macrophage-mediated [^{195}Au]AuNP clearance (LT-MC) are specified.

Parameters of the intratracheal [^{195}Au]AuNP aerosol inhalation and deposition: inhaled aerosol volume, ^{195}Au activity, and deposited ^{195}Au activity (ILD) and its fraction relative to inhaled activity, and the corresponding [^{195}Au]-AuNP mass and number. Furthermore, the fast [^{195}Au]AuNP MCC fraction during the first 2 days, expressed as a fraction of ILD, is rapidly reducing the ILD. This leads to the smaller initially deposited peripheral lung dose (IPLD). In addition, LT-MC fraction of [^{195}Au]AuNP are given, calculated based on fecal excretion and retention in the GIT from day 3−28 p.e.

The estimated deposited [^{195}Au]AuNP fraction relative to the inhaled aerosol shows considerable intersubject variability, indicating that the tidal aerosol volume calculated from eq 3 of Supporting Information is only a rough estimate, presumably due to leakages between the trachea and the endotracheal tube. In addition, these data are lower than the totally deposited fraction of 0.62 as calculated by the MPPD software 3.04 and shown in Figure S4 of Supporting Information. This deviation may be due to the low-pressure ventilation in the plethysmograph chamber[39] (for details, see Supporting Information). The increasing MCC data from 1 h to 4 h clearly show that MCC is very fast. The MCC data are derived from fecal excretion measurements during the first 2 days p.e. of the 7 d and 28 d group. From the third day on, fecal excretion is assigned to LT-MC. Comparing the MCC data of our study from the 24 h, 7 d, and 28 d groups to the estimated tracheobronchial deposition (TB) predicted by the MPPD model (see Table S1, lower part, Supporting Information), our fractions are about twice as high as the value of 0.12 predicted by the MPPD model. This difference may also be due to the experimental conditions of our intratracheal inhalation exposure.

[^{195}Au]AuNP Retention in the Lungs and BAL. Fractional lung retention and BAL data as well as mass concentrations are shown in Table 4 and in Figure 4. Most [^{195}Au]AuNP are retained in the lungs and a rather constant fraction of about 0.06 was found in the cells of BAL throughout the 28 d study period. Free [^{195}Au]AuNP in BAL fluid diminished rather quickly during the first 24 h to below an IPLD fraction of 0.01. At each BAL, AM were the dominating BAL cell fraction; the neutrophilic cell fraction was always below 2% (see Figure S5 of Supporting Information). On a linear scale (Figure 4B), the effects of [^{195}Au]AuNP clearance are shown more clearly over time.

A least-squares fit of the mean alveolar [^{195}Au]AuNP retention of each group of rats over 28 days p.e. (taken from Table 4, lung retention plus BAL) to a monoexponential decrease yields a half-life of 23 d. For comparison, the body retention calculated from excretion data between 3 and 28 d can also be fitted to a monoexponential decrease and yields a half-life of 28 d (see Supporting Information). These values are much shorter than the 60−70 days half-life frequently reported in the literature.[14,40,41] However, this is caused by two well-known reasons:[40,42] (a) there are basically only three lung retention data points at 24 h, 7 days, and 28 days, and (b) the studied retention period is too short to correctly determine the long-term retention half-life because the monoexponential fit is only a first-order attempt for a retention pattern which continuously declines over time, resulting in an increasing half-life. In the present study body retention data, representing predominantly lung retention and minor contributions of the translocated fractions retained in all secondary organs, tissues, and blood (see Table 4 and Figure S1 of Supporting Information) can be determined from the excretion data collected over a period of 28 days according to eq 1b of Supporting Information. These data confirm that excretion continuously decreases, giving rise to an increased half-life of 28 days as detailed in Supporting Information. The use of radiolabeled [^{195}Au]AuNP allows us to precisely control the nanoparticle dose effectively deposited in the lungs and its redistribution in the whole body of the animals, including fecal and urinary excretions.

Long-Term Macrophage-Mediated [^{195}Au]AuNP Clearance. Nanosized and micrometer-sized particles retained in the peripheral lungs are subject to continuous LT-MC toward ciliated airways and the larynx, where they will be swallowed into the GIT. If neither dissolved in the GIT nor absorbed

DOI: 10.1021/acsnano.8b01826
ACS Nano 2018, 12, 7771−7790

Table 2. Aerosol Parameters (Mean ± SD) of All 2 h Intratracheal Inhalation Studies Performed for the Present Biokinetics Study[a]

group of rats	instrument	1 h	4 h	24 h	7 d	28 d
CMD (nm), mean ± SD of 40 spectra.[b]	SMPS	20.66 ± 0.33	20.85 ± 0.35	21.17 ± 0.23	20.77 ± 0.11	20.66 ± 0.25
CMD (nm) of averaged + extrapolated spectrum[c]	SMPS	18.00	18.50	18.52	18.00	18.70
geometrical standard deviation (GSD) mean ± SD of 40 spectra[b]	SMPS	1.45 ± 0.007	1.45 ± 0.004	1.45 ± 0.019	1.45 ± 0.003	1.45 ± 0.006
GSD of averaged + extrapolated spectrum[c]	SMPS	1.45	1.45	1.45	1.45	1.45
number concn (# × 10^6/cm^3)[c]	SMPS	8.46 ± 0.65	8.69 ± 0.71	8.68 ± 0.77	8.58 ± 0.64	8.35 ± 0.64
number concn (# × 10^6/cm^3)	CPC	9.97 ± 0.32	9.64 ± 0.43	10.06 ± 0.46	10.31 ± 0.52	9.84 ± 0.38
median diameter (nm) of volume concn	SMPS	31.39 ± 0.78	31.48 ± 0.41	32.38 ± 2.2	31.56 ± 0.49	31.35 ± 0.49
volume concn[d] (× 10^{-3}; cm^3/m^3)	SMPS	0.082 ± 0.01	0.085 ± 0.01	0.093 ± 0.02	0.084 ± 0.01	0.080 ± 0.01
specific ^{195}Au aerosol activity on filter (kBq/L)[e]	γ-spectrometer	1.74	1.62	1.65	1.68	1.54
derived specific AuNP aerosol mass concn (filter) (μg/L)[f]	γ-spectrometer	1.11	1.04	1.06	1.08	0.99
specific [195Au]AuNP aerosol mass (μg/L)[g]	filter sample	1.65	1.53	1.56	1.59	1.46
mean specific ^{195}Au activity AuNP (MBq/mg) filter act/(vol × dens)	filter, SMPS, γ-spectrometer	1.65	1.53	1.56	1.59	1.46
mean AuNP aerosol number concn (filter) (# × 10^7/L)[f]	filter, SMPS, γ-spectrometer	1.73	1.62	1.64	1.63	1.49
estimated porous AuNP density[g] (g/cm^3)	filter, SMPS, γ-spectrometer	12.90	12.90	12.90	12.90	12.90

[a]Footnote to the table: Data were analyzed using the Aerosol Instrument Manager Software of TSI Inc. version 7.2.5.0 for the scanning mobility particle spectrometer (SMPS). [b]Mean of count median diameters (CMD) and geometric standard deviations (GSD) of all 40 SMPS spectra measured in the size range 10 nm -420 nm. [c]CMD and GSD of the number size spectrum averaged over all 40 SMPS spectra and mean-square fitted and extrapolated to 1 nm size; see Supporting Information. [d]Integral particle volume concentration (PVC) of the aerosol distribution (cm^3/m^3) SMPS derived. [e]Specific ^{195}Au aerosol activity determined from an aerosol filter sample continuously collected during each 2 h exposure at 0.3 L/min aerosol flow according to eq 2 of Supporting Information. [f]Derived AuNP aerosol mass concentration (μg/L) dividing the specific ^{195}Au aerosol activity (filter, kBq/L) by the specific [^{195}Au]AuNP activity concentration 1.55 kBq/μg of the electrodes of the spark ignition aerosol generator. [g]The apparent porous AuNP density was estimated based on the measured aerosol volume concentrations and the derived AuNP aerosol mass concentrations and averaged for all five inhalation exposure experiments.

Table 3. Summary of the Aerosol Inhalation Parameters and Basic Results of the Biokinetics Study[a]

time point after inhalation	1 h	4 h	24 h	7 d	28 d
inhaled aerosol volume (L)[b]	53.05 ± 1.72	51.62 ± 2.33	55.76 ± 3.35	53.16 ± 1.19	59.71 ± 1.28
inhaled ^{195}Au activity (kBq)[b]	92.28 ± 2.99	83.46 ± 3.76	92.02 ± 5.53	89.17 ± 1.99	91.86 ± 1.96
initially deposited ^{195}Au activity A(ILD) (kBq)[b]	47.97 ± 17.99	19.8 ± 4.52	48.54 ± 14.1	36.7 ± 14.54	28.97 ± 9.97
initially deposited fraction (of inhaled activity)[b]	0.52 ± 0.19	0.24 ± 0.05	0.51 ± 0.14	0.41 ± 0.16	0.31 ± 0.11
deposited AuNP mass (μg)[b]	30.73 ± 11.53	12.69 ± 2.9	31.1 ± 9.04	23.51 ± 9.32	18.56 ± 6.39
deposited AuNP number (× 10^{12})[b]	3.82 ± 1.43	1.69 ± 0.38	4.1 ± 1.19	3.14 ± 1.25	2.83 ± 0.92
mucociliary cleared fraction relative to A(ILD)[c]	0.041 ± 0.016	0.209 ± 0.037	0.217 ± 0.088	0.263 ± 0.067	0.311 ± 0.075
deposited alveolar [^{195}Au]AuNP fraction relative to A(IPLD)[b]	0.947 ± 0.031	0.779 ± 0.038	0.775 ± 0.098	0.739 ± 0.079	0.679 ± 0.089
long-term macrophage-mediated cleared fraction relative to A(ILPD)[c]				0.151 ± 0.017	0.382 ± 0.071

[a]Footnotes to the table: according to eqs 4−14 of Supporting Information. [b]Parameters of the intratracheal [^{195}Au]AuNP aerosol inhalation and deposition: inhaled aerosol volume, ^{195}Au activity, and deposited ^{195}Au activity (ILD) and its fraction relative to inhaled activity and the corresponding [195Au]AuNP mass and number. [c]The fast [^{195}Au]AuNP MCC fraction during the first two days, expressed as a fraction of ILD, is rapidly reducing the ILD. This leads to the smaller initially deposited peripheral lung dose (IPLD). In addition, LT-MC fraction of [^{195}Au]AuNP are given, calculated based on fecal excretion and retention in the GIT from day 3−28 p.e.

across the gut walls, they are excreted in feces. Hence, fecal [^{195}Au]AuNP excretion represents clearance from the alveolar region because hepato-biliary particle clearance (HBC) is usually a minute clearance pathway after inhalation at low concentrations of low-toxicity aerosols because (a) only a minor fraction of particles accumulate in the liver (see Table 4) and (b) only a tiny fraction of the particles retained in the liver is cleared via HBC. However, immediately after particle deposition in the thoracic region of the respiratory tract, LT-MC is superimposed by MCC of [^{195}Au]AuNP from the ciliated, conducting airways as shown in Table 3 and Figure 5. Once the MCC fraction is excreted, daily fecal excretion is dominated by rates declining from 0.06 to 0.01 d^{-1} of IPLD out of the peripheral lungs with a delay of about 1−3 days according to the time required for [^{195}Au]AuNP passage through the GIT. Figure 5A shows the daily fecal excretion including MCC, with its delayed maximum at day 2 p.e. When the fractional fecal [^{195}Au]AuNP excretion rates are normalized to the contemporary [^{195}Au]AuNP lung retention in Figure 5B, these rates (diamonds, dashed curve), starting from 4 days p.e., agree rather well with the predicted rates of 0.02−0.03/d obtained for micrometer-sized particles[43] as well as for 20 nm [^{192}Ir]IrNP.[14]

In Figure 6 the daily urinary excretion is plotted based on the data retrieved from the rats of the 7 d and the 28 d groups. During the first 5 days, p.e. urinary excretion rates are very low with a daily excretion fraction of ≤0.0001 (IPLD). Surprisingly, this rate increases up to day 12 to a maximum

DOI: 10.1021/acsnano.8b01826
ACS Nano 2018, 12, 7771−7790

Table 4. Lung Retention and Biodistribution Data in Secondary Organs, Blood, and Tissues Like Carcass[a]

		retention time				
organ	fraction	1 h (mean ± SEM)	4 h (mean ± SEM)	24 h (mean ± SEM)	7 days (mean ± SEM)	28 days (mean ± SEM)
total lungs	corrected	0.989 ± 0.016	0.985 ± 0.002	0.989 ± 0.016	0.798 ± 0.041	0.432 ± 0.032
total lungs	fract. concn [1/g]	0.74 ± 0.028	0.756 ± 0.032	0.708 ± 0.047	0.595 ± 0.04	0.29 ± 0.022
total lungs (× 10^3)	mass concn [ng/g]	21.92 ± 8.34	7.61 ± 1.98	15.39 ± 8.16	10.29 ± 3.78	3.68 ± 1.2
total lungs (× 10^{11})	numb. concn (#/g)	27.7 ± 10.54	10.26 ± 2.66	23.41 ± 7.59	13.83 ± 5.08	5.39 ± 1.79
lav. lungs	corrected	0.771 ± 0.071	0.86 ± 0.046	0.915 ± 0.057	0.74 ± 0.05	0.386 ± 0.033
lav. lungs	fract. concn [1/g]	0.629 ± 0.067	0.72 ± 0.026	0.712 ± 0.074	0.602 ± 0.05	0.279 ± 0.022
lav. lungs (× 10^3)	mass concn [μg/g]	19.01 ± 7.99	7.25 ± 1.85	15.57 ± 8.51	10.38 ± 3.76	3.62 ± 1.35
lav. lungs (× 10^{11})	numb. concn (#/g)	24.03 ± 10.1	9.77 ± 2.5	23.62 ± 8	13.94 ± 5.05	5.3 ± 1.98
BAL cells	corrected[b]	0.059 ± 0.029	0.072 ± 0.053	0.082 ± 0.031	0.055 ± 0.016	0.044 ± 0.04
BAL cells	fract. concn [1/g]	5.865 ± 2.924	7.24 ± 5.279	6.815 ± 4.313	5.481 ± 1.634	4.44 ± 4.009
BAL cells (× 10^5)	mass concn [ng/g]	1.5 ± 0.38	0.71 ± 0.47	1.35 ± 0.51	0.97 ± 0.54	0.48 ± 0.26
BAL cells (× 10^{13})	numb. concn (#/g)	1.89 ± 0.49	0.95 ± 0.63	2.15 ± 1.65	1.3 ± 0.73	0.7 ± 0.38
BAL fluid	corrected[b]	0.16 ± 0.028	0.053 ± 0.015	0.007 ± 0.003	0.003 ± 0.002	0.002 ± 0.002
BAL fluid	fract. concn [1/g]	1.597 ± 0.278	0.526 ± 0.147	0.057 ± 0.042	0.031 ± 0.02	0.017 ± 0.021
BAL fluid (× 10^3)	mass concn [ng/g]	44.83 ± 12.96	5.59 ± 2.85	1.11 ± 0.92	0.61 ± 0.52	0.16 ± 0.11
BAL fluid (× 10^{11})	numb. concn (#/g)	56.67 ± 16.38	7.53 ± 3.84	1.95 ± 1.68	0.82 ± 0.7	0.24 ± 0.17
trach. + bron.	corrected[b]	0.017 ± 0.007	0.011 ± 0.009	0.008 ± 0.004	0.003 ± 0.001	0.005 ± 0.002
trach. + bron.	fract. concn [1/g]	0.15 ± 0.15	0.11 ± 0.06	0.04 ± 0.03	0.02 ± 0.02	0.02 ± 0.01
trach. + bron. (× 10^2)	mass concn [ng/g]	48.2 ± 61.52	10.89 ± 8.06	6.73 ± 4.29	3.68 ± 4.35	2.45 ± 1.74
trach. + bron. (× 10^{11})	numb. concn (#/g)	6.09 ± 7.78	1.47 ± 1.09	1.23 ± 0.71	0.49 ± 0.58	0.36 ± 0.26
liver (× 10^{-3})	corrected	0.124 ± 0.144	0.202 ± 0.113	0.161 ± 0.076	3.335 ± 3.316	5.966 ± 2.337
liver (× 10^{-3})	fract. concn [1/g]	0.018 ± 0.021	0.03 ± 0.017	0.02 ± 0.009	0.402 ± 0.385	0.696 ± 0.278
liver	mass concn [ng/g]	0.52 ± 0.79	0.31 ± 0.22	0.4 ± 0.33	8.27 ± 10.89	9.14 ± 5.1
liver (× 10^8)	numb. concn (#/g)	0.66 ± 1.01	0.43 ± 0.29	0.64 ± 0.33	11.12 ± 14.64	13.4 ± 7.47
liver (× 10^{-3})	transloc. NP fract.	22.1 ± 30.6	13.8 ± 8.2	76.3 ± 85.1	351 ± 188.2	222.5 ± 149.9
spleen (× 10^{-3})	corrected	0.006 ± 0.008	0.004 ± 0.001	0.01 ± 0.005	0.198 ± 0.038	0.567 ± 0.192
spleen (× 10^{-3})	fract. concn [1/g]	0.014 ± 0.019	0.012 ± 0.003	0.022 ± 0.01	0.454 ± 0.066	1.373 ± 0.453
spleen	mass concn [ng/g]	0.44 ± 0.76	0.12 ± 0.03	0.42 ± 0.41	7.99 ± 3.79	18.39 ± 10.88
spleen (× 10^8)	numb. concn (#/g)	0.56 ± 0.96	0.17 ± 0.05	0.72 ± 0.4	10.74 ± 5.1	26.96 ± 15.94
spleen (× 10^{-3})	transloc. NP fract.	1.18 ± 1.87	0.28 ± 0.06	4.62 ± 5.38	28.48 ± 19.73	21.01 ± 15.14
kidneys (× 10^{-3})	corrected	0.009 ± 0.01	0.011 ± 0.003	0.01 ± 0.006	0.058 ± 0.02	0.338 ± 0.063
kidneys (× 10^{-3})	fract. concn [1/g]	0.005 ± 0.006	0.006 ± 0.001	0.005 ± 0.003	0.032 ± 0.009	0.16 ± 0.033
kidneys	mass concn [ng/g]	0.15 ± 0.22	0.06 ± 0.01	0.09 ± 0.02	0.58 ± 0.36	1.95 ± 0.43
kidneys (× 10^7)	numb. concn (#/g)	1.99 ± 2.86	1.02 ± 0.17	1.63 ± 0.58	7.92 ± 4.87	28.81 ± 6.36
kidneys (× 10^{-3})	transloc. NP fract.	1.5 ± 1.98	0.76 ± 0.19	4.22 ± 3.92	8.15 ± 5.64	11.4 ± 5.09
heart (× 10^{-6})	corrected	0.76 ± 0.7	6.82 ± 5.51	16.02 ± 29.42	0.97 ± 0.27	3.57 ± 0.99
heart (× 10^{-6})	fract. concn [1/g]	0.89 ± 0.81	8.76 ± 7.26	18.09 ± 32.4	1.67 ± 1.1	4.12 ± 0.99
heart	mass concn [ng/g]	0.02 ± 0.01	0.07 ± 0.05	0.23 ± 0.32	0.02 ± 0.01	0.05 ± 0.02
heart (× 10^6)	numb. concn (#/g)	2.92 ± 1.5	11.34 ± 6.43	32.58 ± 37.79	4.03 ± 0.83	9.41 ± 3.13
heart (× 10^{-3})	transloc. NP fract.	0.13 ± 0.11	0.44 ± 0.34	4.1 ± 6.05	0.16 ± 0.14	0.13 ± 0.08
brain (× 10^{-6})	corrected	37.4 ± 48.5	3.731 ± 1.345	2.521 ± 3.15	1.259 ± 1.256	1.125 ± 0.391
brain (× 10^{-6})	fract. concn [1/g]	20.3 ± 25.2	2.071 ± 0.745	1.352 ± 1.704	0.72 ± 0.671	0.606 ± 0.206
brain	mass concn [ng/g]	0.443 ± 0.391	0.02 ± 0.006	0.017 ± 0.021	0.015 ± 0.019	0.007 ± 0.002
brain (× 10^7)	numb. concn (#/g)	5.61 ± 4.94	0.29 ± 0.07	0.33 ± 0.25	0.21 ± 0.26	0.13 ± 0.03
brain (× 10^{-3})	transloc. NP fract.	4.83 ± 3.72	0.25 ± 0.06	0.44 ± 0.38	0.13 ± 0.07	0.04 ± 0.01
uterus (× 10^{-3})	corrected	0.012 ± 0.021	0.007 ± 0.005	0.003 ± 0.002	0.004 ± 0.005	0.012 ± 0.002
uterus (× 10^{-3})	fract. concn [1/g]	0.02 ± 0.036	0.013 ± 0.009	0.005 ± 0.003	0.007 ± 0.008	0.019 ± 0.004
uterus	mass concn [ng/g]	0.34 ± 0.46	0.13 ± 0.11	0.06 ± 0.04	0.15 ± 0.23	0.24 ± 0.09
uterus (× 10^7)	numb. concn (#/g)	4.35 ± 5.87	1.83 ± 1.53	1.4 ± 0.7	2.13 ± 3.06	3.7 ± 1.29

DOI: 10.1021/acsnano.8b01826
ACS Nano 2018, 12, 7771−7790

Table 4. continued

organ	fraction	retention time 1 h (mean ± SEM)	4 h (mean ± SEM)	24 h (mean ± SEM)	7 days (mean ± SEM)	28 days (mean ± SEM)
uterus (× 10^{-3})	transloc. NP fract.	0.73 ± 0.91	0.47 ± 0.35	1.36 ± 2.28	0.4 ± 0.24	0.4 ± 0.18
tot. blood (× 10^{-6})	corrected[b]	10.91 ± 6.32	87.07 ± 6.04	34.52 ± 21.43	32.69 ± 6.08	107.1 ± 21.5
tot. blood (× 10^{-6})	fract. concn [1/g]	0.81 ± 0.46	6.72 ± 0.58	2.44 ± 1.41	2.45 ± 0.43	7.21 ± 1.55
tot. blood	mass concn [ng/g]	0.025 ± 0.02	0.067 ± 0.014	0.039 ± 0.014	0.044 ± 0.022	0.088 ± 0.02
tot. blood (× 10^{7})	numb. concn (#/g)	0.314 ± 0.257	0.902 ± 0.188	0.781 ± 0.573	0.585 ± 0.302	1.29 ± 0.338
tot. blood (× 10^{-3})	transloc. NP fract.	3.28 ± 3.62	5.93 ± 0.67	14.12 ± 15.02	4.62 ± 2.89	3.53 ± 1.59
carcass (× 10^{-3})	corrected	10.34 ± 15.96	14.47 ± 2.08	11.19 ± 15.45	4.42 ± 4.13	6.17 ± 4.39
carcass (× 10^{-3})	fract. concn [1/g]	0.06 ± 0.09	0.09 ± 0.01	0.06 ± 0.09	0.04 ± 0.03	0.05 ± 0.03
carcass	mass concn [ng/g]	1.06 ± 0.92	0.9 ± 0.13	0.77 ± 1.1	0.61 ± 0.66	0.6 ± 0.52
carcass (× 10^{9})	numb. concn (#/g)	0.18 ± 0.16	0.12 ± 0.02	0.14 ± 0.15	0.07 ± 0.08	0.08 ± 0.07
carcass	transloc. NP fract.	0.96 ± 0.04	0.98 ± 0.01	0.89 ± 0.11	0.34 ± 0.08	0.16 ± 0.04
skeleton (× 10^{-3})	corrected	0.11 ± 0.07	0.18 ± 0.13	0.08 ± 0.13	0.16 ± 0.09	0.31 ± 0.04
skeleton (× 10^{-4})	fract. concn [1/g]	0.054 ± 0.035	0.089 ± 0.068	0.034 ± 0.056	0.073 ± 0.043	0.132 ± 0.015
skeleton	mass concn [ng/g]	0.149 ± 0.098	0.085 ± 0.053	0.066 ± 0.063	0.136 ± 0.13	0.171 ± 0.071
skeleton (× 10^{7})	numb. concn (#/g)	1.89 ± 1.24	1.15 ± 0.71	0.68 ± 0.6	1.84 ± 1.75	2.53 ± 1.03
skeleton (× 10^{-1})	transloc. NP fract.	0.3 ± 0.26	0.12 ± 0.09	0.13 ± 0.12	0.19 ± 0.12	0.1 ± 0.05
soft tissue (× 10^{-3})	corrected	10.2 ± 16	14.3 ± 2.1	11.1 ± 15.3	4.3 ± 4.1	5.9 ± 4.4
soft tissue (× 10^{-3})	fract. concn [1/g]	0.054 ± 0.083	0.083 ± 0.014	0.054 ± 0.076	0.023 ± 0.021	0.028 ± 0.021
soft tissue	mass concn [ng/g]	0.93 ± 0.86	0.82 ± 0.15	0.66 ± 0.96	0.37 ± 0.42	0.36 ± 0.34
soft tissue (× 10^{8})	numb. concn (#/g)	1.18 ± 1.31	1.036 ± 0.998	1.236 ± 1.282	0.497 ± 0.568	0.527 ± 0.499
soft tissue	transloc. NP fract.	0.93 ± 0.06	0.96 ± 0.01	0.88 ± 0.12	0.4 ± 0.17	0.16 ± 0.07
2nd organs (× 10^{-3})	corrected	0.19 ± 0.02	0.24 ± 0.01	0.21 ± 0.01	3.6 ± 0.23	6.9 ± 0.16
2nd organs (× 10^{-3})	fract. concn [1/g]	0.015 ± 0.017	0.02 ± 0.01	0.015 ± 0.007	0.263 ± 0.232	0.475 ± 0.162
2nd organs	mass concn [ng/g]	0.41 ± 0.57	0.21 ± 0.13	0.3 ± 0.23	5.32 ± 6.66	6.23 ± 3.23
2nd organs (× 10^{8})	numb. concn (#/g)	0.52 ± 0.72	0.28 ± 0.17	0.45 ± 0.21	7.15 ± 8.94	9.13 ± 4.74
2nd organs (× 10^{-1})	transloc. NP fract.	0.31 ± 0.39	0.17 ± 0.08	0.92 ± 0.97	3.89 ± 2.05	2.56 ± 1.68
translocat. (× 10^{-3})	corrected	10.56 ± 16.09	14.83 ± 2.07	11.45 ± 15.55	12.36 ± 11.23	37.44 ± 23.02
translocat. (× 10^{-3})	fract. concn [1/g]	0.068 ± 0.103	0.101 ± 0.014	0.069 ± 0.095	0.075 ± 0.063	0.217 ± 0.126
translocat.	mass concn [ng/g]	1.22 ± 1.06	0.99 ± 0.13	0.87 ± 1.19	1.17 ± 0.98	2.79 ± 2.24
translocat. (× 10^{8})	numb. concn (#/g)	1.77 ± 1.54	1.55 ± 0.19	1.77 ± 1.77	1.85 ± 1.51	4.68 ± 3.71
translocat.	transloc. NP fract.	1	1	1	1	1
total urine (× 10^{-3})	corrected[b]	0	0	0.01 ± 0.01	4.3 ± 7.4	24.22 ± 20.47

[a]For all secondary organs, blood, skeleton and soft tissues at 28d pe the ranking order according to first line "corrected" and the fifth line "transloc. NP fract." is liver > soft tissue > spleen > kidneys > skeleton > blood > uterus > heart > brain. However, this ranking order changes for the lines "fract. concn" for "mass concn" and "numb. concn" per mass of organ or tissue to spleen > liver > kidneys > soft tissue > skeleton > uterus > blood > heart > brain. [^{195}Au]AuNP retention in lungs including BAL data and in secondary organs and tissues 1 h, 4 h, 24 h, 7 d, and 28 d after intratracheal inhalation. In each first line of a given organ, fractional data were corrected for fast clearance and the [^{195}Au]AuNP content in residual blood after exsanguination (corrected). After these corrections, the ^{195}Au activity data were converted into [^{195}Au]AuNP concentrations per mass of organ or tissue as IPLD fraction per gram (g^{-1}) or as nanoparticle mass per organ mass in gram ($ng{\cdot}g^{-1}$) or as number of particles per organ mass in gram ($\#/g^{-1}$). In the fifth line of each secondary organ or tissue, fractions are normalized to the total of those [^{195}Au]AuNP which had crossed the ABB (transloc. NP fract., see eq 24 of Supporting Information). Carcass and soft tissue are defined in Table S2 of Supporting Information; briefly, the carcass contains the rest of the body without the tabulated organs, tissues, and skin; soft tissue is carcass without skeleton. Note the varying exponents in brackets of the left column are used to ensure an adequate number of valid digits. Below the table the ranking orders of secondary organs and tissues are provided at day 28 pe. Mean ± SEM of $n \geq 4$ rats/time point. Note, graphical displays of data of lines 2, 6, and 3 of each organ or tissue are shown in Figure 10 and Figure S7 of Supporting Information, respectively. [b]Correction for residual blood is not applicable.

of about 0.002 (IPLD), followed by a continuous decrease to 0.0002 at the end of the observation period after 28 days.

Because urinary excretion follows renal clearance, these amounts have to be attributed to [^{195}Au]AuNP that have reached the blood. To further investigate this effect in Figure 7, the distribution of the translocated [^{195}Au]AuNP in various secondary organs and tissues are presented as stacked columns for the various retention time points until the end of the observation period after 28 days. Strikingly, during the first 24 h, the dominant fraction of translocated [^{195}Au]AuNP is found in soft tissue. Thereafter, not only the fractions in liver, spleen, and kidneys increase but even more so the integral urinary

DOI: 10.1021/acsnano.8b01826
ACS Nano 2018, 12, 7771−7790

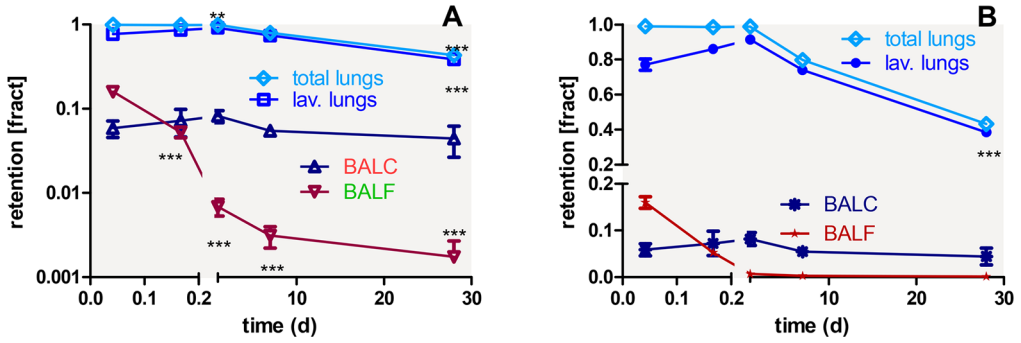

Figure 4. (A,B) Logarithmic + linear *y*-axis, respectively. Retention of intratracheally inhaled [^{195}Au]AuNP in the total lungs between 1 h and 28 d; the recoveries in BAL cells (BALC) and BAL fluid (BALF) are shown separately. The data are given as fractions of IPLD, *i.e.*, corrected for fast [^{195}Au]AuNP MCC. Data are given as mean ± SEM (standard error of the mean), $n \geq 4$ rats/time point. Data in all panels are corrected for [^{195}Au]AuNP retained in the residual blood volume of the lungs; statistical significances *versus* data of 1 h: $p < 0.01$ (**), $p < 0.001$ (***).

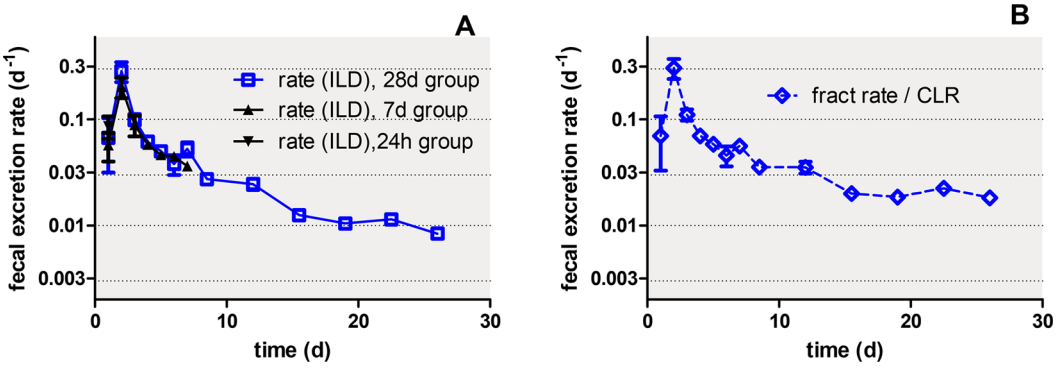

Figure 5. (A) Daily fecal excretion rates of intratracheally inhaled [^{195}Au]AuNP representing predominant MCC from conducting thoracic airways and fecally excreted during the first 2 days p.e. and thereafter from the alveolar region. The fecal excretion rates were normalized to ILD. Data of the groups of rats analyzed after 24 h, 7 d, and 28 d are presented. For the 28 d group, integral fecal samples over 3−4 days are divided by the number of sample days and assigned to the mean day of the sample interval. (B) The diamond symbols represent the excretion rates that are normalized to the contemporary lung retention (CLR) at each time point (see eq 1 in Supporting Information). The resulting exponential equation with the half-life is given in eq 1. Mean ± SEM, $n \geq 5$ rats per time point.

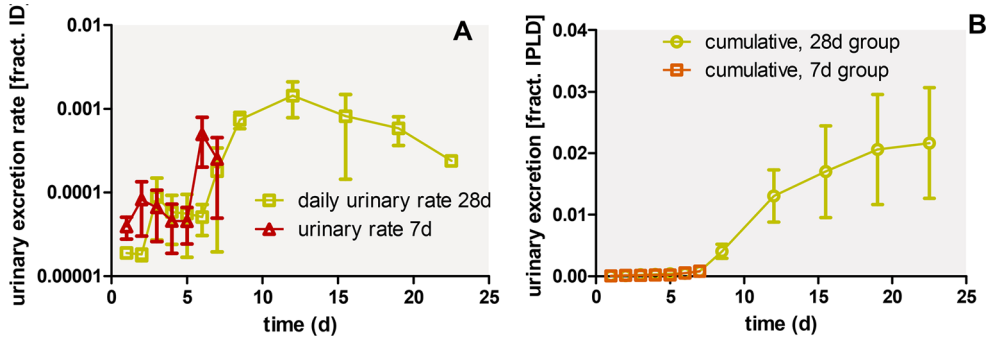

Figure 6. (A) Daily urinary excretion of intratracheally inhaled [^{195}Au]AuNP of the groups of rats analyzed after 7 d and 28 d. Data are given as mean fractions of IPLD (±SEM). (B) Mean cumulative urinary excretion (± SEM). For the 28 d group, the integral urine samples collected over 3−4 days are divided by the number of sampling days and assigned to the mean day of the sample interval. Mean ± SEM, $n \geq 5$ rats per time point.

excretion, which becomes the predominant fraction after 28 days (see also the last subsection of R&D below).

NP Relocation into the Interstitium and Re-entrainment Back onto the Epithelial Surface. NP relocation from the lung epithelium to interstitial spaces and re-entrainment back to the epithelium for LT-MC to the larynx and GIT is not well-known, and a comprehensive assessment of particle relocation has not been made for micrometer-sized particles in the rat lungs. Therefore, we present arguments based on our own experimental observations and on literature references:

1. We observed that only a small fraction of AuNP is lavageable by BAL from day 1 p.e. until the end of the study; this is in contrast to that of micrometer-sized particles as shown by refs 17,18. However, immediately after inhalation (*i.e.*, 1 h p.e.), we proved that we can

DOI: 10.1021/acsnano.8b01826
ACS Nano 2018, 12, 7771−7790

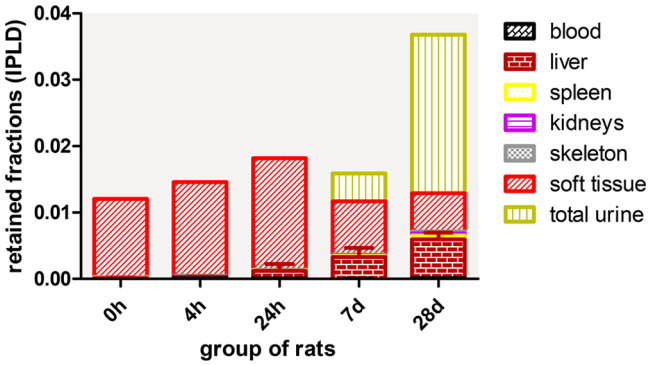

Figure 7. [^{198}Au]AuNP translocated across the ABB presented as stacked columns with contributions from major secondary organs, soft tissue, and cumulative urine. While translocated [^{198}Au]AuNP accumulated predominantly in soft tissue up to 24 h, the fraction released in urine increases rapidly from day 7 to day 28 p.e. Mean ± SEM, $n \geq 4$ rats per time point.

indeed lavage major fractions of free AuNP from the epithelium.

2. The review of Lehnert[44] and papers by Adamson and Bowden[45−47] provide evidence that EC1 can endocytose NP at the epithelial side and eventually exocytose those toward the basolateral side. More recently, Thorley and co-workers[48] provided evidence for prominent NP uptake by EC1 while they ruled out uptake by alveolar epithelial type 2 cells (EC2) and also the passage by paracellular transport. They stated that NP uptake occurs preferably by diffusive processes into the cytoplasm, which allow for exocytosis and transport across the basal membrane into the interstitium as supported by our study. In our collaborative studies,[30,49] we demonstrated the localization of AuNP and TiO_2-NP in interstitial spaces by TEM.
3. According to Nunn[50] and Weibel,[51] the cytoplasmic leaflets of EC1 provide the largest portion of their surface area on the basal membrane which separates the adjacent vascular endothelial cells to allow unhindered gas exchange. Yet, our data up to 24 h do not support the notion that [^{195}Au]AuNP cross EC1 at both the "active site of gas exchange"[50] and the basal membrane because any NP exocytosis would lead to rather rapid uptake by vascular endothelial cells and translocation into the circulation which we did not observe. Instead the translocated [^{195}Au]AuNP fraction to blood was rather small during the first 24 h.
4. Hence, EC1 either exocytose directly into septal interstitial spaces, which provide only a relative small surface area at the side of EC1 and/or the exocytosed NP migrate in between the basal membrane and the EC1membranes to the next septal interstitial space. Once there, NP may be phagocytized by interstitial macrophages (IM), fibroblasts, *etc.* Referring to ref 45,53, there is a large population of IM such that the role of IM in phagocytizing NP and long-term retention in the septal interstitial spaces appears plausible.
5. For gradual re-entrainment back onto the epithelium, Lehnert[44] reviewed the pathway of IM onto the epithelium. In addition, IM and fibroblasts may exchange their NP-load with AM like in a relay.

[^{195}Au]AuNP relocation from the epithelial surface was assessed, as outlined in the Supporting Information, distinguishing between (a) free [^{195}Au]AuNP suspended in the BALF, (b) [^{195}Au]AuNP associated or taken up by freely moving macrophages in BALC, and (c) lung retained [^{195}Au]AuNP fractions already bound and/or taken up by cells of the epithelial barrier and beyond in the interstitium that cannot be recovered from the lungs by lavage. Already 1 day p.e., almost no free [^{195}Au]AuNP were found in BALF but lavaged [^{195}Au]AuNP were predominantly phagocytized by AM (Table 4). [^{195}Au]AuNP fractions in BALC and BALF are snapshots of currently retained AuNP on the epithelium resulting from the dynamics of arriving AuNP due to the interstitial re-entrainment and exiting AuNP due to LT-MC. (In Figure 6B, daily LT-MC per CLR is shown.) In the Supporting Information, we derive the estimated [^{195}Au]AuNP fractions in the total AM-pool of the lungs from the measured BALC fractions.[14] Both are normalized to the contemporary [^{195}Au]AuNP lung retention (CLR), thereby obtaining fractions independent of earlier clearance. The fractions in the AM-pool, shown in Figure 8, remain roughly constant

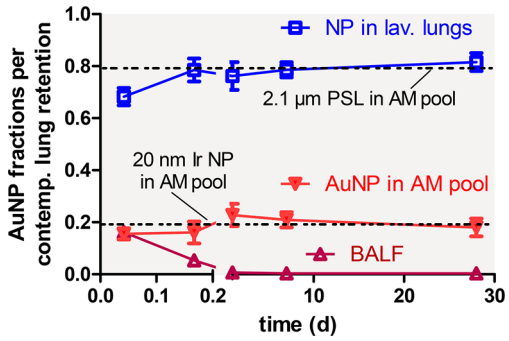

Figure 8. [^{195}Au]AuNP fractions of fractions of the total AM pool[14] (see Supporting Information; red triangles downward) derived from the experimentally determined kinetics of lavageable [^{195}Au]AuNP fractions associated with BALC. Additionally, [^{195}Au]AuNP fractions found in the interstitium, estimated from [^{195}Au]AuNP fractions of lavaged lungs (blue squares). Fractions are normalized to CLR from 1 h to 28 d p.e. Additionally, the fractions of free [^{195}Au]AuNP in BALF are presented which decline rapidly (crimson triangles upward). These data are compared with averaged fractions of 20 nm [^{192}Ir]IrNP in the total AM pool[14,15] (lower dashed line) and with those of 2.1 μm PSL particles in the total AM pool[18] (upper dashed line). Data points are mean ± SEM; $n \geq 4$ rats per time point.

throughout 28 days p.e. at fractions of about 0.2 while fractions of about 0.8 are retained in the lung interstitium and cannot be recovered by BAL. Differential cell counts of the various cell types found in each BAL are shown in Figure S5 of the Supporting Information.

We cannot exclude NP passage through bronchus-associated lymphoid tissue (BALT) at bronchioles−alveolar duct junctions back onto the bronchiolar epithelium.[46,52,53] However, BALT plays an important immunogenic role for fluid absorbed from the alveolar surface, and the reverse flow onto the epithelial surface was postulated in the literature but not proven.[50,51] Furthermore, there are only about 30−50 BALT sites in the rat lungs,[44,54] which are far too few required for NP re-entrainment because LT-MC clearance is the most prominent clearance mechanism eliminating most of the long-term retained NP within 28 days.

DOI: 10.1021/acsnano.8b01826
ACS Nano 2018, 12, 7771−7790

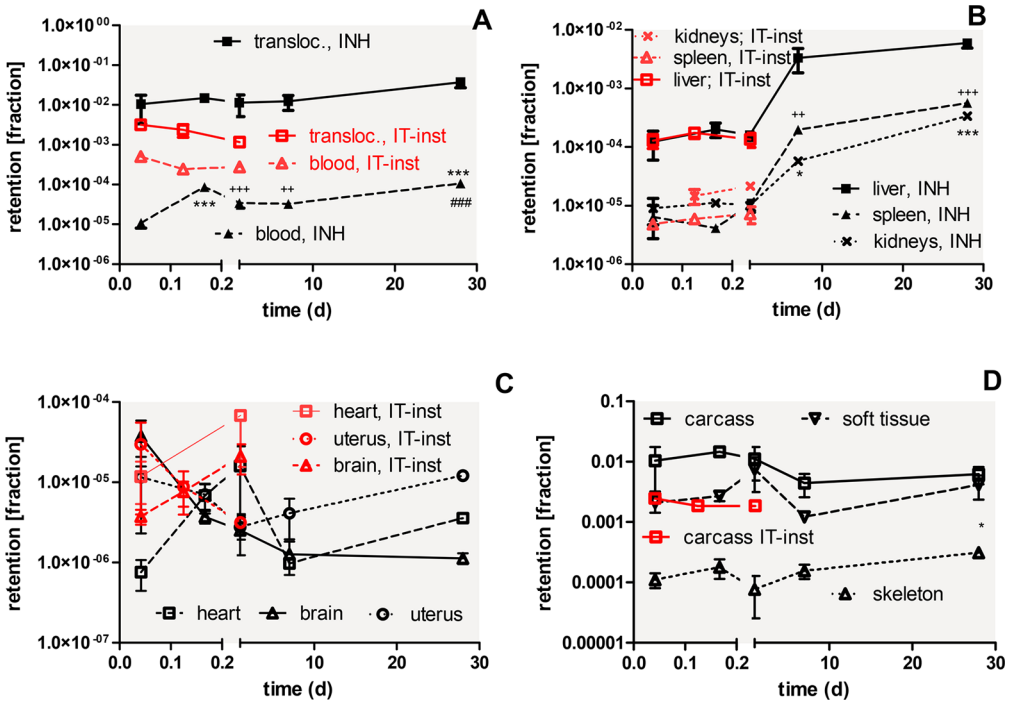

Figure 9. Retained fractions of intratracheally inhaled [^{195}Au]AuNP investigated up to 28 days. (A) Total translocation and blood; (B) liver, spleen, and kidneys; (C) heart, brain, and uterus; (D) carcass, soft tissue, and skeleton. [^{195}Au]AuNP retention is given as fractions of IPLD. For comparison, the retention data (fractions of IPLD) between 1 h and 24 h after intratracheal instillation of S-TTP surface-modified, monodisperse 18 nm [^{198}Au]AuNP are included. Data in all panels are corrected for [^{195}Au]AuNP retained in the residual blood volume of organs and tissues. Mean ± SEM, $n \geq 4$ rats per time point. Statistical significances: $p < 0.05$ (*), $p < 0.01$ (**), $p < 0.001$ (***); (A) * 7 d vs 4 h and 28 d; +++, ++ 4 h vs 24 h and 7 d; ### 28 d vs 24 h and 7 d, (B) *** 28 d vs all; * 1 h vs 1 h 24 h; $^{+++}$ 28 d vs 1 h, 24 h, 7 d; $^{+2}$ 7 d vs 0 h, 24 h. (D) Skeleton: * 24 h vs 28 d.**

The kinetics of translocated [^{195}Au]AuNP into interstitial spaces and their re-entrainment back onto the lung epithelium is similar to our previous findings over six months after inhalation of a radiolabeled 20 nm iridium ([^{192}Ir]IrNP) aerosol. Hence, because the fractions of AM-mediated clearance toward the larynx remain constant over 28 days (or 180 days for the [^{192}Ir]IrNP), this indicates that the interstitially retained [^{195}Au]AuNP gradually reappear onto the lung epithelium as we have described previously for [^{192}Ir]-IrNP.[14,15] These findings differ from earlier observations after administration of much bigger 2.1 μm polystyrene latex particles (PSL) in rats[18] and of 1.3 μm sized fused alumino-silicate particles (FAP) inhaled by hamsters,[17] where fractions of 0.8 (relative to the contemporary lung burden) of both micrometer-sized particle materials were accessible to BAL over six months, and only a small fraction (0.2) of micrometer-sized particles could not be recovered by BAL. Therefore, two different nanoparticle materials, gold and iridium, of similar size (20 nm) but with different morphologies, spheroid-shaped [^{195}Au]AuNP and chain-aggregated [^{192}Ir]IrNP, were first effectively relocated into the interstitium of rat lungs, but subsequently they were gradually re-entrained back onto the lung epithelium for LT-MC toward the larynx. In contrast, the two types of spherical micrometer-sized particles were mainly retained in AM on the alveolar epithelium of either rats or hamsters and were gradually cleared by LT-MC. Thus, for micrometer-sized particles and nanoparticles LT-MC is the prominent clearance pathway (Table 3) while translocation across the ABB and subsequent distribution in secondary organs and tissues represents a minor clearance pathway for NP in the rat lungs (Figure 9A) but has not been reported for micrometer-sized particles.

[^{195}Au]AuNP in Trachea and Main Bronchi: Lymph Node Accumulation and/or Transient Mucociliary Transport. [^{195}Au]AuNP clearance may also happen via the lymphatic system of the lungs which not only drains to the tracheobronchial and hilar lymph nodes and eventually to the jugular vein but also via mediastinal lymph nodes toward the thoracic duct and into the circulation. Over decades, efficient particle accumulation in the lymph nodes at the first bifurcation and along the trachea has been described and holds also for NP.[55] Therefore, we analyzed the [^{195}Au]AuNP content in the trachea, first bifurcation and both main bronchi, including tiny and therefore barely detectable hilar lymph nodes, at each retention time point. The retention of [^{195}Au]AuNP in these "tracheal samples" may be caused by three mechanisms: (a) gradual [^{195}Au]AuNP accumulation in the hilar lymph nodes and along the trachea, (b) [^{195}Au]AuNP on the airway epithelium in transit toward the larynx as a result of mucociliary clearance first by MCC and later by LT-MC, and (c) prolonged retention in the tracheal epithelium as observed in human studies showing a slow clearance, particularly, for submicrometer particles and NP.[56−59] Retention data of tracheal samples are compiled in Table 4 for all groups of rats.

In eq 26 of Supporting Information, we estimate the contribution of transient mucociliary transported [^{195}Au]AuNP at time points from 4 h to 28 d p.e. Compared with the observed retention data for trachea and main bronchi reported in Table 4, the transitional [^{195}Au]AuNP fractions in the tracheal sample are at least 10-fold lower, indicating that the

DOI: 10.1021/acsnano.8b01826
ACS Nano 2018, 12, 7771−7790

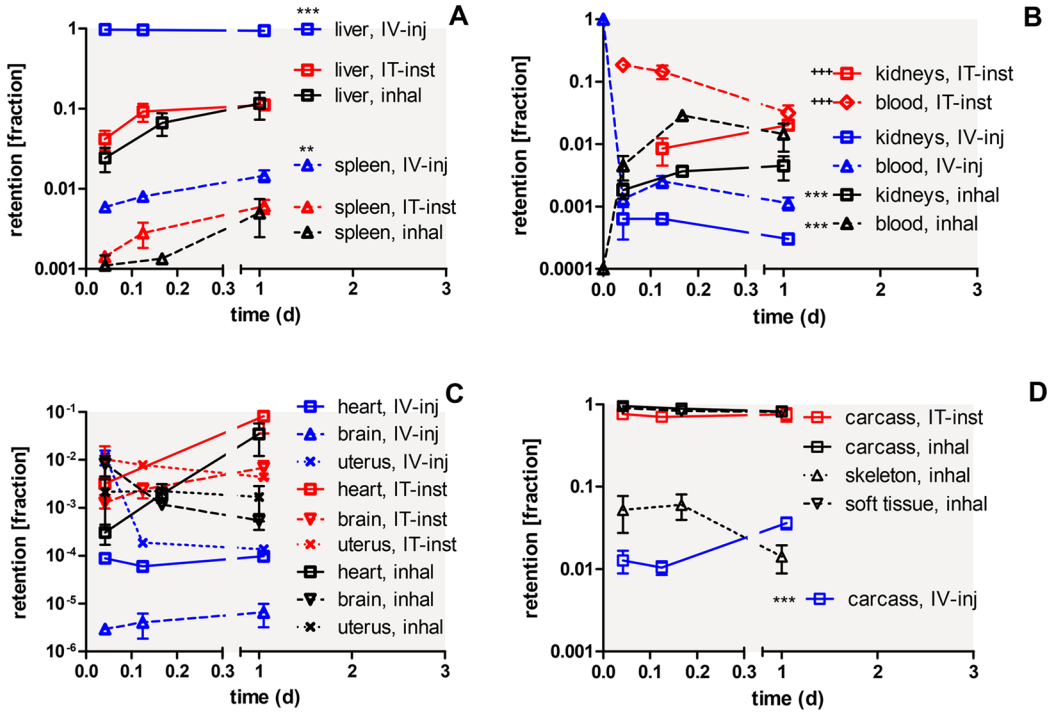

Figure 10. Comparison of the retained fractions of inhaled 20 nm [^{195}Au]AuNP with monodisperse, IT-instilled 18 nm [^{198}Au]AuNP[20] and with IV injected 18 nm [^{198}Au]AuNP. While inhaled [^{195}Au]AuNP and IT instilled [^{198}Au]AuNP are normalized to the sum of all AuNP that translocated across the ABB, the IV injected [^{198}Au]AuNP are normalized to the initial dose (ID). Only data up to 24 h are available due to the short half-life of the ^{198}Au isotope. (A) Liver and spleen; (B) kidneys, blood; (C) heart, brain, uterus; (D) carcass, soft tissue, skeleton. Data are corrected for [^{195}Au]AuNP retained in the residual blood volume of organs and tissues. Mean ± SEM, n = 4 rats per time point. Statistical significances: $p < 0.05$ (*), $p < 0.01$ (**), $p < 0.001$ (***). (A) Liver, * IV vs INH and IT; spleen, **, IV vs INH and IT. (B) Kidneys and blood, *** INH vs IT; $^{+++}$ IT vs IV. (D) Carcass, *** IV vs INH and IT.**

contribution of [^{195}Au]AuNP in transit is rather low. Hence, the major amount of the measured [^{195}Au]AuNP in the tracheal samples are either retained in lymphoid tissue according to mechanism (b) or in the airway epithelium according to mechanism (c).

The fact that the highest fractions of tracheal samples occurred immediately after the 2 h inhalation (1 h retention time point), and after 4 h, and decreased thereafter does not support [^{195}Au]AuNP accumulation in lymph nodes but suggests a role of epithelial [^{195}Au]AuNP retention. This notion is supported by a previous Wistar rat study after a single 1 h inhalation of monodisperse 0.7, 1.0, or 1.5 μm sized, radiolabeled fused alumino-silicate particles[60] in which rather low particle fractions of 0.0002 (of ID) were determined in tracheobronchial and hilar lymph nodes. In addition, subchronic 13-week exposure studies using aerosols of submicrometer agglomerates of ultrafine TiO_2 NP at doses of 0.5, 2, or 10 mg/m^3 showed also very low accumulation in tracheobronchial and hilar lymph nodes of the rats of the low-dose groups (data close to detection limit) during the entire recovery period of 52 weeks. Lymph node uptake was however 100-fold higher at the end of the high dose exposure and increased steeply during the recovery period.[20] In summary, the tracheal fractions being highest in the 1 h and 4 h groups of rats suggest epithelial [^{195}Au]AuNP retention while 24 h until 28d fractions may comprise both epithelial retention in trachea and main bronchi and to a lesser extent [^{195}Au]AuNP lymphoid accumulated retention.

Biokinetics of Translocated [^{195}Au]AuNP into Secondary Organs and Tissues. In Table 4, [^{195}Au]AuNP retention in the lungs and in all secondary organs and tissues are presented as mean ± SEM for all time points 1 h, 4 h, 24 h, 7 d, and 28d p.e. Data are given as fractions and mass concentrations of the IPLD, thus excluding the fast cleared [^{195}Au]AuNP fraction from the conducting lung airways by MCC as described in Supporting Information.

In Figure 9, [^{195}Au]AuNP retention data in secondary organs and tissues are shown as fractions of the IPLD, taken from the first line of each organ in Table 4. These data are compared during the first 24 h with those obtained from intratracheally instilled, monodisperse 18 nm [^{198}Au]AuNP radio-labeled with the short-lived ^{198}Au isotope. [^{198}Au]AuNP were surface modified with sulfonated triphenylphosphine (S-TPP).[18] Figure 9A shows an increase of the total amount of [^{195}Au]AuNP translocated across the ABB from 0.012 to 0.036 and fractions circulating in blood increasing 10-fold from 0.00001 to 0.0001. Compared with the translocation of monodisperse 18 nm [^{198}Au]AuNP after IT-instillation, the fractions are similar after 1 h but diverge during the next 24 h. The monodisperse 18 nm [^{198}Au]AuNP fractions after IT instillation are about 10-fold higher in blood. Similarly, in Figure 9B, during the first four hours the MPS of liver, spleen, and kidneys accumulate small fractions of 2×10^{-4}, 4×10^{-6}, and 1×10^{-5} inhaled [^{195}Au]AuNP, respectively. These data are remarkably similar to those of the previously intratracheally instilled [^{198}Au]AuNP in terms of absolute fractions and trends. Subsequently, the retained [^{195}Au]AuNP fractions in these organs increase 30-fold (140-fold in spleen) until 28 d p.e. Figure 9C shows that the AuNP fractions in the uterus after inhalation and IT instillation are similar and rather

DOI: 10.1021/acsnano.8b01826
ACS Nano 2018, 12, 7771−7790

constant over time. In the heart, a maximum is reached 24 h after inhalation and IT instillation. It can be clearly noted that almost all translocated [^{195}Au]AuNP accumulate in the carcass (Figure 9A,D) and only 50-fold less accumulate in secondary organs (Figure 9B,C and Table 4). In the carcass (Figure 9D), the [^{195}Au]AuNP fractions remain rather constant during the first 24 h, but after inhalation those fractions are almost 10-fold higher than after IT instillation. Beyond 24 h, the inhaled [^{195}Au]AuNP fraction declines gradually until 28 d. In the carcass, the retention is dominated by a major fraction in soft tissue. The [^{195}Au]AuNP fraction in soft tissue is rather constant over time and about 20 times higher than in the skeleton. We also note the more than 10-fold increase of [^{195}Au]AuNP in liver, spleen, and kidneys (Figure 9B) 24 h p.e. which was not found in heart, brain, or uterus (Figure 9C) and the slight decline in carcass (Figure 9D).

Compared with the deposition dose rate achievable by inhalation, the deposition dose rate in IT instillation experiments is very high and provides an additional suspension fluid volume which has to be resorbed by the epithelium. Furthermore, the [^{195}Au]AuNP applied in the present inhalation study did not undergo any surface modification after their generation by spark ignition and the subsequent heat treatment, while the instilled [^{198}Au]AuNP were surface-modified with S-TPP molecules for colloidal stabilization in aqueous suspension. Thus, different dose rates, different surface properties, and the differences between nanoparticles in aerosol and suspension may have contributed to the different transient biokinetics observed during the first four hours. However, after 24 h, all secondary organ fractions agree surprisingly well, indicating an adaptive response of the lungs and/or changes in the surface modification of the S-TPP coated [^{198}Au]AuNP. Also, the [^{198}Au]AuNP fractions in blood that were initially 100-fold higher than those after-[^{195}Au]AuNP inhalation converge to some extent after 24 h; in contrary IT-instilled [^{198}Au]AuNP, carcass fractions remain 10-fold lower than those after[^{195}Au]AuNP inhalation. The similarity of both biokinetics in secondary organs after 24 h can be considered as an *in vivo* confirmation of previous *in vitro* observations in various cultured cells[61−63] which found evidence that the TPP-surface molecules are rapidly replaced by proteins and biomolecules of the culture medium. If this applies to the epithelial lining fluid (ELF) and its surfactant, then the instilled [^{198}Au]AuNP lost their initial TPP surface molecules and gained an equally modified, biomolecular *in vivo* surface corona as the initially "naked" inhaled [^{195}Au]AuNP which mediates a similar biokinetics after 24 h.

Inhaled or IT-Instilled AuNP Fractions in Secondary Organs and Tissues Relative to Those AuNP Which Had Crossed the ABB: a Comparison to the Fate of IV-Injected AuNP. Both sets of data in Figure 9 are strikingly different from those after IV injection of [^{198}Au]AuNP[22] as shown in Figure 10. Unlike the fractions normalized to IPLD in Figure 9, the lung-administered AuNP fractions in Figure 10 are presented relative to the translocated AuNP across the ABB in order to directly compare organ and tissue accumulation with AuNP in the circulation after IV injection. In our studies, IV injection yields the highest initial AuNP concentration in blood but this declines 500-fold during the first hour because the MPS of the liver demonstrates its high capacity of effectively scavenging most of the IV injected [^{198}Au]AuNP. Thereafter, IV injected [^{198}Au]AuNP are 100-fold and 30-fold lower than the translocated fractions of circulating [^{198}Au]AuNP after IT instillation or after [^{195}Au]AuNP inhalation, respectively (Figure 10B). Surprisingly, almost all translocated AuNP after both modes of lung administration are observed in the carcass, *i.e.*, predominantly in soft tissue, and the translocated fractions retained in the liver are more than 10-fold lower than after IV injection. The IV injected [^{198}Au]AuNP in the spleen are only 3-fold higher than those translocated fractions of the lung-administered AuNP. Lung administered translocated AuNP fractions in kidneys are rather similar (Figure 10B), but they are 10-fold higher than those of IV injected [^{198}Au]AuNP.

In this initial phase, free IV injected [^{198}Au]AuNP will most likely have bound to highly abundant blood proteins/biomolecules such as albumin, *etc.* depending on the surface chemistry and structure of the AuNP. This may modulate the interactions between AuNP and membrane receptors of the MPS cells of a given organ or tissue. The poorly efficient MPS cells of blood are saturated, taking up only a small [^{198}Au]AuNP fraction. Yet, AuNP uptake from circulating blood is governed by the cells of the MPS in each of the various organs and tissues.[23] More surprising is that inhaled as well as IT instilled AuNP, which only gradually translocated across the ABB into blood resulting in low blood concentrations, cause only low liver accumulation but highest accumulation in soft tissue in terms of the total amount of [^{198}Au]AuNP per organ or tissue. [Note: based on [^{198}Au]-AuNP per gram of organ or tissue the concentration fractions of soft tissue are certainly much lower as shown in Table 4.] This indicates that the scavenging MPS cells of the liver that recognize IV injected [^{198}Au]AuNP with high efficiency do almost not recognize the AuNP that reached the blood after crossing the ABB. In contrast, the MPS cells and maybe other cells of the soft tissue (which includes the vasculature of blood and lymphatic drainage) do recognize the lung-applied and translocated AuNP. In other words, the lung-applied AuNP which translocated across the ABB were either (a) surface modified by biomolecules immediately in the lungs and/or (b) in the blood after passage through the ABB. Alternatively, it may be conceivable that (c) the AuNP were transported by blood cells, *e.g.*, phagocytes, monocytes, lymphocytes, thrombocytes after endocytosis, or even by erythrocytes after adhesion to their surface membrane. While there is sufficient literature providing a phenomenological description of NP interactions with these cell types, until now no quantitative assessment is available. The complexity of the plethora of biomolecules potentially involved in corona formation as well as the manifold of NP-cell−receptor interactions hampers a better understanding which is urgently needed for any NP application in nanomedicine and drug delivery. In fact, this lack of knowledge may be one of the underlying reasons for the limited successes of nanomedicinal applications of nanoparticles so far. Our biokinetics data also clearly demonstrate the invalidity and impracticability of IV injection studies using suspended NP as surrogate approaches to study the biokinetics and toxic responses of inhaled or IT instilled NP. The same conclusion was drawn from our recent biokinetics studies after IT instillation *versus* IV injection of 70 nm sized TiO_2-NP.[26,27]

After 24 h until 28 d, p.e. translocated fractions of inhaled [^{195}Au]AuNP in liver, spleen, and kidneys increase about 10-fold (Table 4, respective lines 6), while the translocated fractions in the carcass (*i.e.*, predominantly in soft tissue) and also in heart and brain decline by an order of magnitude. These changes indicate ongoing redistribution from the latter organs/

DOI: 10.1021/acsnano.8b01826
ACS Nano 2018, 12, 7771−7790

tissues to the former organs, besides urinary excretion. Only in the skeleton and the uterus fractions remain constant over time suggesting little redistribution.

When considering the [^{195}Au]AuNP concentrations per mass of organ or tissue, concentrations in the carcass (*i.e.*, predominantly in soft tissue) are again highest and close to 0.0001 of IPLD/g over the entire 28 d period (Table 4 and Figure S7A,D in Supporting Information). The [^{195}Au]AuNP concentrations per weight of liver, spleen, kidneys, uterus, and skeleton are about 10-fold lower and remarkably similar at about 0.00001 of IPLD/weight during the first 24 h p.e. This may indicate similar MPS cells densities and similar kinetics of phagocytic uptake in liver, spleen, kidneys, and uterus. After 24 h, concentrations in liver, spleen, and kidneys increase more than 10-fold until 28 d, indicating continuous [^{195}Au]AuNP net accumulation with time. In the uterus, soft tissue, and skeleton, they remain rather constant over time, indicating no net changes over 28 d. In contrast, brain concentrations drop by almost 100-fold, suggesting substantial [^{195}Au]AuNP clearance over time. The [^{195}Au]AuNP concentration per blood mass remains at least 5-fold lower than most of the organ or tissue concentrations.

The delayed increase in [^{195}Au]AuNP fractions in liver, spleen, kidneys, and uterus 24 h p.e. (Figure 10B,C; Table 4) coincide with the delayed increase in the daily urinary excretion starting only 5−6 days p.e., reaching a maximum of a 10 times higher rate at 12 d p.e. In urinary excretion, most likely the smallest particles are successfully passing renal clearance while larger ones might accumulate in the kidneys, as discussed below.

Surprisingly, the translocated fractions of IT instilled [^{198}Au]AuNP in the brain increase from 0.001 to 0.007 (corresponding to an AuNP number of 5×10^4 to 3.5×10^5) within 24 h while the translocated fractions of inhaled [^{195}Au]AuNP in the brain decline from 0.008 to 0.0005 (corresponding to an AuNP number of 2×10^7 to 7×10^5). However, all these fractions and corresponding AuNP numbers are higher than after IV injection of [^{198}Au]AuNP, where only fractions of about 3×10^{-6} (corresponding to an AuNP number of 1.5×10^4) of the translocated particles were found in the brain.[22]

Contribution of AuNP Absorbed in the GIT to the Biokinetics in Secondary Organs and Tissues. Previously, we have shown that 24 h after gavage of monodisperse 18 nm [^{198}Au]AuNP the GIT-absorbed fraction was about 0.002 (ID).[21] Multiplying these small fractions with the MCC fraction in Table 3 indicates that translocation across the ABB is superimposed by an [^{198}Au]AuNP absorbed fraction of 0.0005 due to their passage through the GIT. However, this fraction is very small compared with the ABB translocation of about 0.01 during the first 24 h. Because of the short half-life of ^{198}Au, no additional data for GIT-absorbed [^{198}Au]AuNP fractions had been determined. Similarly, GIT-absorbed fractions of 0.002 and 0.001 were found 24 h and 7 days after gavage of 70 nm TiO_2-NP,[64] respectively. These data were used to estimate the contribution of GIT absorption resulting from MCC and LT-MC in addition to the translocation across the ABB of the same intratracheally instilled 70 nm TiO_2-NP.[27] Generally, the GIT-absorbed TiO_2-NP contributed modestly within a 1−10% range to the accumulation and retention in secondary organs and tissues. GIT absorption of 18 nm [^{198}Au]AuNP was similar to that of 70 nm TiO_2-NP during the first 24 h. Therefore, it appears plausible that the evaluated contribution of GIT-absorbed TiO_2-NP of 1−10% over 28 d can be applied as a rough estimate of the GIT-absorbed contribution to the biokinetics of [^{195}Au]AuNP after inhalation.

[^{195}Au]AuNP Dissolution Dynamics or Renal Clearance of Disagglomerated [^{195}Au]AuNP? Although a gradual dissolution of metallic nanoparticles (leading to the presence of metal ions followed by fast renal clearance) cannot generally be excluded *in vivo*, this hypothesis is extremely unlikely in the case of gold nanoparticles that exhibit an extraordinary stability under a variety of environmental conditions. [Citrate stabilized [^{195}Au]AuNP exhibit free Au ions in the range of a few 10^{-6} even after 1.5 years storage, which result from an incomplete reaction of the $AuHCl_3$ used for the NP synthesis. In other words, the reaction yield was better than 99.999% in this case.] In a previous study,[20] we compared the biokinetics of intratracheally instilled, radiolabeled ionic $^{198}Au^{3+}$ with the biokinetics of a suite of six differently sized, monodisperse, intratracheally instilled AuNP radiolabeled with ^{198}Au, ranging from 1.4 to 200 nm. On the basis of this study, which included 18 nm sized [^{198}Au]AuNP, very similar to the 20 nm [^{195}Au]AuNP used in the present study, we may discard the hypothesis of AuNP dissolution because ^{198}Au found in urine was negligible and, moreover, because soluble ionic ^{198}Au showed a very different biokinetics pattern[20] compared to that of [^{198}Au]AuNP. The urinary excretion of $^{195}Au^{3+}$ would be very fast and a delayed onset of accelerated nanoparticle dissolution just 5 days p.e., matching the onset of increasing urinary excretion in Figure 6 does not appear plausible.

The cumulative content of [^{195}Au]AuNP in urine increased very slowly during the first week p.e. up to a fraction of 0.0033, although already 4 h p.e. one-third of the finally translocated fraction after 28 d was stored predominantly in soft tissue (Figure 7). Thereafter, cumulative urinary excretion increased steeply and amounted to 0.025 after 28 days (Figure 6B and Table 4). Such a biphasic excretion pattern has not been previously reported. On the other hand, there is evidence that renal clearance is strongly size-dependent with a NP size threshold at 5−6 nm beyond which renal clearance rapidly diminishes.[11,65−69] It should be noted, that only 24 h data are available and high NP doses were IV administered in the cited studies. Our previous biokinetics study[20] after intratracheal instillation of monodisperse 1.4, 2.8, 5.0 and 18 nm [^{198}Au]AuNP showed that translocation across the ABB during the first 24 h decreased rapidly with increasing NP size from 0.039, 0.0031, 0.020, and 0.0020, respectively. Most of these [^{198}Au]AuNP were stored in the body, with highest fractions in the carcass followed by kidneys and liver, but they were not rapidly cleared *via* urine.

The simplest explanation that the smallest [^{195}Au]AuNP of the size distribution may be subject to renal translocation cannot account for the cumulative urinary excretion of 2.5% of IPLD because the ^{195}Au activity measurements correspond to the mass of [^{195}Au]AuNP and the total [^{195}Au]AuNP mass being smaller than 6−8 nm accounts to less than 0.3% in original the log-normal size distribution. However, this fraction might be underestimated because it is based on the extrapolation of a pure log-normal distribution to values below the measurement threshold of 10 nm. In the case that the size distribution exhibits a Gaussian contribution, such an extrapolation would underestimate the contributions of the smaller particles significantly. Whether such a Gaussian contribution is present and whether it could account for a

DOI: 10.1021/acsnano.8b01826
ACS Nano 2018, 12, 7771−7790

factor of nearly 10 is uncertain and would require much more sophisticated measurements of the size distribution. However, also another effect could offer an explanation. It may be possible that in the current study the fraction of smallest [^{195}Au]AuNP < 6−8 nm of the original aerosol spectrum together with disagglomeration of the inhaled [^{195}Au]AuNP occurred and that both were translocated across the ABB and stored in the body. [Note the heat treatment of the [^{195}Au]AuNP aerosol at 600 °C did not melt the gold nanoparticles to perfect spheres but provided "potato-shaped" nanoparticles. Furthermore, the apparent density of the [^{195}Au]AuNP was derived to be $^{2}/_{3}$ of the bulk density of 19.5 g/cm^3, indicating pronounced porosity (see Table 2), which might allow for some disaggregation of the [^{195}Au]-AuNP.] At this point, we can only speculate about the observed delayed onset of increasing renal clearance after 1 week. For example, it could be due to (a) retarded ABB translocation of larger fragments or intact [^{198}Au]AuNP or (b) enhanced renal release after a certain threshold concentration of the accumulating fragments in the kidneys. Yet these speculations can only serve to trigger other future investigations including more sophisticated size distribution measurements.

A delayed maximum of urinary excretion was so far not reported for rodent inhalation studies using AuNP. However, a recent human AuNP inhalation study by Miller and co-workers[13] indeed points toward a delayed urinary excretion pattern based on inhaled 17 nm AuNP. The mean urinary excretion increased from 35 ng/L after 24 h to about 60 ng/L after three months. According to corrected dose calculations submitted later,[70] they estimated in their first study an initial urinary excretion rate of 0.02%/d which increased after three months to 0.04%/d. In their second inhalation study using again AuNP of a CMD of 17 nm,[13] they reported lower initial urinary excretion concentrations close to the detection limit of 2 ng/L, which, however, increased almost 10-fold to 18 ng/L after 28 days, corresponding to fractional rates of 0.001%/d at 24 h and 0.01%/d after 28 d. In this human study, the AuNP aerosol was generated by the same spark ignition method but the AuNP aerosol was not heat treated in contrast to the [^{195}Au]AuNP used in the present study. The authors claim to have EM analyzed the primary particles of the aerosolized AuNP (17 nm median diameter measured by an SMPS) to be of a size of 4 nm and speculate that renal clearance and urinary excretion was probably dominated by those primary 4 nm particles which might have become disagglomerated from the 17 nm AuNP in the human lungs. They obtained more evidence for their speculation by an additional human inhalation experiment in the same paper[13] in which heat treated AuNP of a CMD of 52 nm were applied which were not detectibly excreted in urine. The urinary excretion observed in the human study is indeed close to our present observations.

In addition, disagglomeration and subsequent enhanced translocation across the ABB of initially agglomerated, inhaled AuNP of 45 nm size consisting of either 7 nm Au primary particles when compared to 20 nm Au primary particles was described previously by Balasubramanian and co-workers.[10] Finally, it needs to be emphasized that urinary excretion of NP < 5−6 nm is confirmed by several papers, mostly in rodents.[65,67−69]

CONCLUSION

Intratracheal inhalation of gold nanoparticles (AuNP) by negative pressure ventilation caused anisotropic deposition, preferably in the caudal lungs independent of the rat age. However, the pulmonary concentration of the deposited AuNP was low before, high at, and medium after postnatal day 21. This finding correlates very well with the development of the anatomical structure[36] and pulmonary particle retention.[19] About 30% AuNP were deposited on airway epithelia, resulting in rapid mucociliary clearance and swallowing into the GIT.

From the alveolar region, AuNP clearance is dominated by long-term alveolar macrophage-mediated clearance (LT-MC) of 38% of initial peripheral lung deposit (IPLD) after 28 days p.e. Compared to LT-MC, AuNP-translocation across the air−bloo -barrier or *via* lymphatic drainage were much smaller. Air−blood barrier translocation into blood circulation occurred already during the first 24 h and led to persistent retentions in secondary organs and tissues: the highest retention in liver is not surprising, but the second highest in soft tissue (comprising of muscle, connective tissue, fat, skin) is noteworthy because it is not determined in many other studies.

The biokinetics data of the present study are remarkably similar to those obtained after intratracheal instillation of 18 nm AuNP but drastically different with respect to data obtained after IV injection of 18 nm AuNP.

The intratracheally inhaled AuNP deposit mainly in the rat alveolar region and relocate rapidly into the epithelium/interstitium to be cleared mainly by LT-MC toward the larynx. Comparing the urinary excretion dynamics of the human study after the inhalation of similar sized AuNP[13] with data obtained from our healthy adult rats, there is surprising agreement suggesting similar translocation dynamics across the air−blood barrier in both species.

MATERIALS AND METHODS

Study Design. The first part of this study comprises a deposition distribution study performed on healthy, female Wistar−Kyoto rats of different ages from newborn to adulthood on postnatal days 7, 14, 21, 35, 60, and 90. One rat of each age was inhalation exposed with the ^{195}Au radiolabeled AuNP aerosol. Rats were exsanguinated and dissected immediately after the 2 h exposure.

In the second part, the biokinetics was studied in adult, healthy, female Wistar−Kyoto rats (8−10 weeks old, with a mean of 60 days). Rats inhaled the same ^{195}Au radiolabeled AuNP aerosol for 2 h, and the biodistributions were analyzed in at least four rats for each time-point, *i.e.*, immediately after 2 h inhalation (corresponding to a mean retention time of 1 h (n = 5), 4 h (n = 4), 24 h (n = 6), 7 d (n = 5), and 28 d (n = 5)). Adult female rats were used for comparability with our previous biokinetics studies.

Animals and Maintenance. Healthy, female Wistar−Kyoto rats and two male Wistar−Kyoto rats (WKY/Kyo@Rj rats, purchased from Janvier, Le Genest Saint Isle, France) of various ages were housed in relative humidity and temperature controlled ventilated cages (VentiRack Bioscreen TM, Biozone, Margate, UK) on a 12 hday/night cycle. Rodent diet and water were provided *ad libitum*. After purchase, the rats were adapted for at least 2 weeks and then randomly attributed to the experimental groups (biokinetics study: 8−10 weeks of age, mean body weight 216 ± 14 g; the adult rats for the age dependent study were also purchased and the 90 d rat was kept in our animal facilities until its appropriate age) or they were mated to breed the newborn rats to be used in the aerosol deposition distribution study at ages of 7 d, 14 d, 21 d or 35 d. For this age-dependent deposition distribution study, one rat of each age was inhalation exposed with the [^{195}Au]AuNP aerosol.

DOI: 10.1021/acsnano.8b01826
ACS Nano 2018, 12, 7771−7790

All experiments on alive animals were carried out in the lab of WGK in Munich. These experiments were conducted under German federal guidelines for the use and care of laboratory animals and were approved by the Regierung von Oberbayern (Government of District of Upper Bavaria, approval no. 55.2-1-54-253 I-26-10) and by the Institutional Animal Care and Use Committee of Helmholtz Centre Munich. Physiological parameters of the rats are given in Table 1.

Synthesis and Characterization of the [^{195}Au]AuNP Aerosol. Radiolabeled AuNP aerosols were produced by spark ignition between two cylindrical gold electrodes (diameter 3 mm, length 4−5 mm) which had been irradiated in the cyclotron at the JRC Ispra (Italy), with protons impinging with about 30 MeV energy on one of the flat ends of each of the two cylinders in order to produce ^{195}Au (186 days half-life, gamma ray emission at 98.9 keV) in the electrode material as described earlier in detail by Möller et al.[71] The [^{195}Au]AuNP aerosol was then generated by spark ignition (GFG100, Palas, Karlsruhe, Germany) at 150 Hz spark frequency between the proton irradiated tips of two adjacent gold electrodes in an argon (Ar) gas stream of 3 L/min. The highly electrically charged aerosol was quasi-neutralized by an inline radioactive ^{85}Kr source and the originally agglomerated [^{195}Au]AuNP passed through a 30 cm long tube furnace kept at a temperature of 600 °C to form single, more spherical and compact 20 nm sized [^{195}Au]AuNP. Passing through a copper tube (inner diameter 8 mm) downstream of the furnace, the aerosol was cooled and then diluted by mixing with humidified oxygen and nitrogen to obtain an oxygen concentration of 20−25% at a flow rate of typically 10 L/min and a relative humidity of about 70% when fed into the inhalation apparatus as described earlier.[71] The aerosol concentration and size distribution was continuously sampled and controlled by a condensation particle counter (CPC 3022A, TSI, Aachen, Germany) and a scanning mobility particle spectrometer (SMPS; consisting of a model 3071 differential mobility analyzer and a model 3010 CPC, TSI, Aachen, Germany). Averages of the CMD, volume median diameters (VMD), and GSD as well as number concentrations and volume concentrations are given as mean ± SD in Table 2. Because the SMPS instrument could measure only to a lower particle size limit of 10 nm, the averaged spectra were fitted to a log-normal size distribution using a least-squares method, and the fits were extrapolated to a size of 1 nm (for details see Supporting Information). These corrections led to slightly lower CMDs of about 19 nm instead of 21 nm, while the GSD changed only negligibly (Table 2). All parameters of the [^{195}Au]-AuNP aerosol freshly generated by spark ignition generation are similar to those previously reported.[71] The specific ^{195}Au activity of the aerosol was determined by γ-spectrometric analysis of absolute filters onto which [^{195}Au]AuNP had been collected at an aerosol flow of 0.3 L/min throughout each exposure period. From the activity deposited on the filter, an activity concentration of the [^{195}Au]AuNP aerosol of 1.55 kBq/μg was derived. This value agrees well with calculations based on experimental reaction cross section data for the production of ^{195}Au *via* proton irradiation of ^{197}Au by assuming a homogeneous activation in a surface layer of 250 μm depth of the gold electrodes.[72]

The geometry of the sampling line to the CPC and SMPS was adjusted to ensure that the aerosol was analyzed at the same aerosol residence time as the time the rats were inhaling from the main aerosol stream passing by the rat inhalation ports (Figure of Supporting Information). The aerosol was fed through a tailor-made rodent inhalation apparatus maintained at an aerosol pressure of about 30 Pa below the laboratory pressure for radiation safety reasons.[73,74] The actual aerosol and [^{195}Au]AuNP inhalation parameters of each group are shown in Tables 2 and 3, respectively.

From the measured aerosol volume concentrations and the derived AuNP aerosol mass concentrations compiled in Table 2, an averaged apparent [^{195}Au]AuNP density of 12.5 ± 0.7 g/cm^3 was derived for all five inhalation exposure experiments. This value is about $^2/_3$ compared to the bulk gold density of 19.5 g/cm^3, resulting from the "potato-like" AuNP shape and/or the porous structures of the agglomerated/aggregated [^{195}Au]AuNP because a complete melting and resolidification of the aggregates formed from the primary particles generated by spark ignition could not be expected from the heat treatment at 600 °C during the passage through the tubular furnace as discussed previously.[71]

Intratracheal Inhalation Exposure. The exposure details for the biokinetics studies have been first described in ref 16 and recently in more detail in the supplementary data of ref 75. Briefly, each rat was anesthetized by intramuscular injection of a mixture of medetomidine (15 μg/100 g body weight), midazolam (0.2 mg/100 g body weight), and fentanyl (0.5 μg/100 μg body weight). Thereafter, they were ventilated individually *via* a flexible endotracheal tube and placed on their left lateral side in a plethysmograph box of our tailor-made inhalation apparatus and connected to the aerosol system (see Figure S2 of Supporting Information). They were exposed to the freshly generated aerosol for 2 h. In the following, this exposure method will be called "intratracheal inhalation".

To study the [^{195}Au]AuNP deposition distributions in the lungs of rats of different age, one rat of each age group was exposed similarly *via* intratracheal inhalation as described above.[75] During the 2 h inhalation, isoflurane was continuously added into the [^{195}Au]AuNP aerosol flow to achieve 1% isoflurane concentration in order to maintain controlled continuous anesthesia during the exposure.

Treatment after Inhalation: Age Dependent Deposition Distribution. Immediately after the 2 h inhalation exposure, each rat was intraperitoneally anesthetized with ketamine (100 mg/100 g body weight) and xylazine (0.5 mg/100 g body weight) and mounted on a 60° tilted surgical board. The [^{195}Au]AuNP exposed lungs were fixed by perfusion of the pulmonary blood vessels *via* the right ventricle with 2.5% glutaraldehyde.[76] The trachea was cannulated and ligated by a flexible catheter (16 G, 2 in) and sealed by a plunger before the thorax was opened in order to remove the inflated lungs. These were immediately transferred into a microwave oven (Moulinex, 1000 W) and connected to a filtered airflow supply that was maintained at a constant pressure of 25 cm water to gently dry the inflated lungs at a tidal volume of 70−75% of total inspiratory capacity (TLC). The microwave oven was run for 10−12 h at the lowest setting (defrost, at which the 1000 W power was turned on intermittently about 10% of the treatment time).[77,78] The deposition distribution was studied afterward using a SPECT gamma camera, computed tomography, and autoradiography making use of the radioactive ^{195}Au label of the 20 nm [^{195}Au]AuNP.

Treatment after Inhalation: Biokinetics of Adult Rats. For the biokinetics studies after the intratracheal inhalation, anesthesia of each rat was antagonized by a subcutaneous injection of a mixture of Atipamezol (0.075 mg/100 g body weight), Flumazenil (20 μg/100 g body weight), and Naloxon (10 μg/100 g body weight) as described earlier.[15,16] Each rat was kept individually in a metabolic cage, and excreta were collected separately and quantitatively. After the first week maintained in a metabolic cage, for ethical reasons the rats of the 28 d group were kept individually in a normal cage on cotton cloths. Each cloth was replaced by a new cloth every 3−4 days, and from each collected cloth fecal droppings were quantitatively separated. After separation, the cloth contained only ^{195}Au originating from urine which had soaked and dried. In Table S1, Supporting Information, the list of collected organs, tissues, body fluids, and excretion are given.

SPECT and Lung Slices Autoradiography. When the lungs were dry and rigid their total radioactivity was determined by γ-spectrometry using a calibrated NaI(Tl) scintillation detector and then they were subjected to a single photon emission computed tomograph (SPECT) scan. For this purpose, the dried lungs were mounted under the pinhole collimator of the SPECT gamma-camera (Prism 2000, Picker, Espelkamp, Germany), and a 3D-SPECT scan was acquired during a full 360° loop (120 images of 300 s each). For a volume scan, the dried lungs were analyzed by a high resolution computer tomograph (HRCT, Somatom, Siemens, Germany) at the Radiology Department of LMU Hospital Großhadern, Munich, Germany. Thereafter, all dried lungs were shipped from the Helmholtz Center Munich to the Institute of Anatomy of the University of Bern, Switzerland, and each right lung was transversally cut in slices of 1.5 mm thickness that were subjected to autoradiography. Sections were exposed to an imaging plate (Fuji

DOI: 10.1021/acsnano.8b01826
ACS Nano 2018, 12, 7771−7790

Film BAS-SR 2025; Raytest, Straubenhardt, Germany) for 15 min, and the images were acquired using a radioluminography laser imager (Fuji Film BAS 1800 II system, Raytest). The autoradiography images were further analyzed using the software Fuji for a quantitative assessment of the signal[79] and compared with the SPECT results.

[^{195}Au]AuNP Relocation into the Epithelium and Interstitial Spaces. Details of the BAL procedure distinguishing between [^{195}Au]AuNP associated with BALC and free [^{195}Au]AuNP in the supernatant BALF are provided in the Supporting Information. To compare the [^{195}Au]AuNP fractions in BALC and BALF with those retained in the lavaged lungs, [^{195}Au]AuNP fractions were normalized to the amount of contemporarily retained [^{195}Au]AuNP in the total lungs (CLR) at each time point, providing lavageable [^{195}Au]AuNP fractions *versus* the intraepithelial and interstitial retained [^{195}Au]-AuNP fractions not accessible to BAL.

[^{195}Au]AuNP in the Trachea and Main Bronchi. Efficient particle retention and accumulation in the hilar lymph nodes at the first bifurcation and along the trachea has been described in many inhalation studies on various species over decades. Therefore, we γ-spectrometrically analyzed the [^{195}Au]AuNP content in the trachea with the first bifurcation and both main bronchi including the hilar lymph nodes at each retention time point.

Evaluation of [^{195}Au]AuNP Biokinetics. At 1 h, 4 h, 24 h, 7 d, and 28 d p.e., rats were anesthetized by 5% isoflurane inhalation followed by intraperitoneal anesthesia with ketamine (100 mg/100 g body weight) and xylazine (0.5 mg/100 g body weight) and euthanized by exsanguination *via* the abdominal aorta. For γ-spectrometry, blood, all organs, tissues, and excretions were collected and ^{195}Au radioactivities were measured without any further physicochemical processing, as detailed in the Supporting Information and in earlier works.[20,20−22] Because by exsanguination only about 70% of the blood volume could be recovered, the residual blood contents of organs and tissues after exsanguination were calculated according to the findings of Oeff and König,[80] and the ^{195}Au radioactivities of the organs were corrected for these contributions in the residual blood volume (for details see eqs 17−23 in Supporting Information).

The data evaluation started with the calculation of the measured ^{195}Au activity values as fractions of the IPLD, calculated as the deposited [^{195}Au]AuNP radioactivity in the lungs minus the fast [^{195}Au]AuNP clearance from the conducting airways in each animal, as derived in eqs 12 and 13 of the Supporting Information. These fractions are averaged over the group of rats and are presented with the SEM. Note that the retention time of the group of rats which was dissected immediately after the 2 hintratracheal inhalation was allocated to a mean retention time of 1 h for the subsequent biokinetics considerations. Throughout this report, nanoparticle quantities are calculated from the ^{195}Au activity determined with γ-scintillation detectors calibrated in γ-ray energy and detection efficiency for ^{195}Au, corrected for background and radioactive decay during the experiments (see Supporting Information). Samples yielding background-corrected counts in the 99 keV region-of-interest of the ^{195}Au γ-spectrum were defined to be below the detection limit (<DL; < 0.01 Bq) when the number of counts was less than three standard deviations from the background counts collected without any sample in the γ-scintillation detector. The detailed execution of these corrections is presented in the Supporting Information. All calculated significances are based on One-Way ANOVA analyses with the posthoc Bonferoni test. In the case of direct comparisons of two groups, the unpaired t test was used. Significance was considered at $p \leq 0.05$.

The current [^{195}Au]AuNP biokinetics after intratracheal inhalation were compared with three studies that applied a suspension of [^{198}Au]AuNP with a size of 18 nm by intratracheal instillation, gavage, or IV injection.[20−22,81] The data of lung-applied nanoparticles were further normalized to the [^{195}Au]AuNP fraction which had translocated across the ABB (see eqs 24 and 25 in the Supporting Information). It should be noted that the [^{198}Au]AuNP were surface modified with S-TPP in contrast to the freshly generated pristine [^{195}Au]AuNP.

ASSOCIATED CONTENT

Supporting Information

The Supporting Information is available free of charge on the ACS Publications website at DOI: 10.1021/acsnano.8b01826.

Aerosol size distribution measurements using SMPS and spectral fitting; lung and body retention fits; age dependent translocation of 30 nm IrNP; intratracheal inhalation exposure to the freshly generated [^{195}Au]-AuNP aerosol; Age Dependent [^{195}Au]AuNP Deposition Distribution; sample preparation for radiometric analysis of biokinetics; radiometric and statistical analysis; BAL relative to CLR, relocation, and re-entrainment; parameters of inhalation and deposition; total [^{195}Au]AuNP deposition in each rat determined by the balanced ^{195}Au activities of the entire dissected rat including its total excretion; ^{195}Au activity determination of skeleton and soft tissue; blood correction and total blood volume; [^{195}Au]AuNP accumulation and retention in secondary organs and tissues relative to translocated [^{195}Au]AuNP across the ABB; [^{195}Au]-AuNP concentration per mass of organ or tissues (1/g) as fractions of IPLD; [^{195}Au]AuNP retention in the trachea and main bronchi (PDF)

AUTHOR INFORMATION

Corresponding Author

*E-mail: kreyling@helmholtz-muenchen.de.

ORCID

Wolfgang G. Kreyling: 0000-0002-0702-6567

Present Addresses

[#]A.W.: Department of Infrastructure, Safety, and Occupational Protection, Helmholtz Zentrum München - German Research Center for Environmental Health, D-85764 Neuherberg/Munich, Germany.

[▽]C.S.: Abteilung Gesundheitsschutz, Berufsgenossenschaft Holz and Metall, Am Knie 8, D-81241 München, Germany

Author Contributions

W.G.K., N.G., and W.M. designed the biokinetics part of the study and AuNP generation; W.G.K. and J.C.S. designed the part of the age dependent deposition distribution study; Radiolabeling of the gold electrodes was designed and performed by U.H. and N.G.; the biological experiments of the study were performed by S.H., W.G.K., W.M., M.S., C.S., J.C.S., and A.W; data evaluation and analysis were performed by N.H., S.H., U.H., W.G.K., W.M., J.C.S., and A.W.; the manuscript was drafted by U.H., W.G.K., W.M., J.C.S.

Notes

The authors declare no competing financial interest.

[†]Dr. Winfried Möller is deceased

ACKNOWLEDGMENTS

We thank S. Kaidel, P. Mayer, and N. Senger from the Helmholtz Center Munich for their excellent technical assistance, as well as A. Bulgheroni, G. Cotogno, and F. Simonelli from the EU-Joint Research Center, who strongly supported the NP radiolabeling task. We also thank M. Behe from the Paul Scherrer Institute (Villigen, Switzerland) for performing the autoradiography measurements. Finally, we are grateful for the critical comments of A. Tsuda from Harvard School of Public Health (Boston, USA). This work was partially supported by the German Research Foundation SPP

DOI: 10.1021/acsnano.8b01826
ACS Nano 2018, 12, 7771−7790

1313, the EU-FP6 project Particle-Risk (012912 (NEST)), and the EU FP7 projects NeuroNano (NMP4-SL-2008-214547), ENPRA (NMP4-SL-2009-228789), and InLiveTox (NMP-2008-1.3-2 CP-FP 228625-2), as well as US-NIH grant HL074022, and Swiss National Science Foundation grants 310030_153468 and 310030_175953.

DEDICATION

All authors mourn the loss of our colleague and good friend Winfried Möller who passed away in August 2017.

REFERENCES

(1) Ciriminna, R.; Falletta, E.; Della Pina, C.; Teles, J. H.; Pagliaro, M. Industrial Applications of Gold Catalysis. *Angew. Chem., Int. Ed.* **2016**, *55*, 14210−14217.
(2) Villa, A.; Dimitratos, N.; Chan-Thaw, C. E.; Hammond, C.; Prati, L.; Hutchings, G. J. Glycerol Oxidation Using Gold-Containing Catalysts. *Acc. Chem. Res.* **2015**, *48*, 1403−1412.
(3) Heo, Y. K.; Bratescu, M. A.; Ueno, T.; Saito, N. Synthesis of Mono-Dispersed Nanofluids Using Solution Plasma. *J. Appl. Phys.* **2014**, *116*, 024302.
(4) Morgan, K.; Burch, R.; Daous, M.; Delgado, J. J.; Goguet, A.; Hardacre, C.; Petrov, L. A.; Rooney, D. W. Application of Halohydrocarbons for the Re-Dispersion of Gold Particles. *Catal. Sci. Technol.* **2014**, *4*, 729−737.
(5) Johnston, H. J.; Hutchison, G.; Christensen, F. M.; Peters, S.; Hankin, S.; Stone, V. A Review of the *in Vivo* and *in Vitro* Toxicity of Silver and Gold Particulates: Particle Attributes and Biological Mechanisms Responsible for the Observed Toxicity. *Crit. Rev. Toxicol.* **2010**, *40*, 328−346.
(6) Khlebtsov, N.; Dykman, L. Biodistribution and Toxicity of Engineered Gold Nanoparticles: A Review of *in Vitro* and *in Vivo* Studies. *Chem. Soc. Rev.* **2011**, *40*, 1647−1671.
(7) Kermanizadeh, A.; Balharry, D.; Wallin, H.; Loft, S.; Møller, P. Nanomaterial Translocation−the Biokinetics, Tissue Accumulation, Toxicity and Fate of Materials in Secondary Organs−a Review. *Crit. Rev. Toxicol.* **2015**, *45*, 837−872.
(8) Hamzawy, M. A.; Abo-Youssef, A. M.; Salem, H. F.; Mohammed, S. A. Antitumor Activity of Intratracheal Inhalation of Temozolomide (Tmz) Loaded into Gold Nanoparticles and/or Liposomes against Urethane-Induced Lung Cancer in Balb/C Mice. *Drug Delivery* **2017**, *24*, 599−607.
(9) Hao, Y.; Altundal, Y.; Moreau, M.; Sajo, E.; Kumar, R.; Ngwa, W. Potential for Enhancing External Beam Radiotherapy for Lung Cancer Using High-Z Nanoparticles Administered Via Inhalation. *Phys. Med. Biol.* **2015**, *60*, 7035−7043.
(10) Balasubramanian, S. K.; Poh, K. W.; Ong, C. N.; Kreyling, W. G.; Ong, W. Y.; Yu, L. E. The Effect of Primary Particle Size on Biodistribution of Inhaled Gold Nano-Agglomerates. *Biomaterials* **2013**, *34*, 5439−5452.
(11) Han, S. G.; Lee, J. S.; Ahn, K.; Kim, Y. S.; Kim, J. K.; Lee, J. H.; Shin, J. H.; Jeon, K. S.; Cho, W. S.; Song, N. W.; Gulumian, M.; Shin, B. S.; Yu, I. J. Size-Dependent Clearance of Gold Nanoparticles from Lungs of Sprague-Dawley Rats after Short-Term Inhalation Exposure. *Arch. Toxicol.* **2015**, *89*, 1083−1094.
(12) Oberdörster, G.; Kuhlbusch, T. A. J. *In Vivo* Effects: Methodologies and Biokinetics of Inhaled Nanomaterials. *NanoImpact* **2018**, *10*, 38−60.
(13) Miller, M. R.; Raftis, J. B.; Langrish, J. P.; McLean, S. G.; Samutrtai, P.; Connell, S. P.; Wilson, S.; Vesey, A. T.; Fokkens, P. H. B.; Boere, A. J. F.; Krystek, P.; Campbell, C. J.; Hadoke, P. W. F.; Donaldson, K.; Cassee, F. R.; Newby, D. E.; Duffin, R.; Mills, N. L. Inhaled Nanoparticles Accumulate at Sites of Vascular Disease. *ACS Nano* **2017**, *11*, 4542−4552.
(14) Semmler-Behnke, M.; Takenaka, S.; Fertsch, S.; Wenk, A.; Seitz, J.; Mayer, P.; Oberdorster, G.; Kreyling, W. G. Efficient Elimination of Inhaled Nanoparticles from the Alveolar Region: Evidence for Interstitial Uptake and Subsequent Reentrainment onto Airways Epithelium. *Environ. Health Perspect.* **2007**, *115*, 728−733.
(15) Semmler, M.; Seitz, J.; Erbe, F.; Mayer, P.; Heyder, J.; Oberdorster, G.; Kreyling, W. G. Long-Term Clearance Kinetics of Inhaled Ultrafine Insoluble Iridium Particles from the Rat Lung, Including Transient Translocation into Secondary Organs. *Inhalation Toxicol.* **2004**, *16*, 453−459.
(16) Kreyling, W. G.; Semmler, M.; Erbe, F.; Mayer, P.; Takenaka, S.; Schulz, H.; Oberdörster, G.; Ziesenis, A. Translocation of Ultrafine Insoluble Iridium Particles from Lung Epithelium to Extrapulmonary Organs Is Size Dependent but Very Low. *J. Toxicol. Environ. Health, Part A* **2002**, *65*, 1513−1530.
(17) Ellender, M.; Hodgson, A.; Wood, K. L.; Moody, J. C. Effect of Bronchopulmonary Lavage on Lung Retention and Clearance of Particulate Material in Hamsters. *Environ. Health Perspect.* **1992**, *97*, 209−213.
(18) Lehnert, B. E.; Valdez, Y. E.; Tietjen, G. L. Alveolar Macrophage-Particle Relationships During Lung Clearance. *Am. J. Respir. Cell Mol. Biol.* **1989**, *1*, 145−154.
(19) Semmler-Behnke, M.; Kreyling, W. G.; Schulz, H.; Takenaka, S.; Butler, J. P.; Henry, F. S.; Tsuda, A. Nanoparticle Delivery in Infant Lungs. *Proc. Natl. Acad. Sci. U. S. A.* **2012**, *109*, 5092−5097.
(20) Kreyling, W. G.; Hirn, S.; Möller, W.; Schleh, C.; Wenk, A.; Celik, G.; Lipka, J.; Schaffler, M.; Haberl, N.; Johnston, B. D.; Sperling, R.; Schmid, G.; Simon, U.; Parak, W. J.; Semmler-Behnke, M. Air-Blood Barrier Translocation of Tracheally Instilled Gold Nanoparticles Inversely Depends on Particle Size. *ACS Nano* **2014**, *8*, 222−233.
(21) Schleh, C.; Semmler-Behnke, M.; Lipka, J.; Wenk, A.; Hirn, S.; Schaffler, M.; Schmid, G.; Simon, U.; Kreyling, W. G. Size and Surface Charge of Gold Nanoparticles Determine Absorption across Intestinal Barriers and Accumulation in Secondary Target Organs after Oral Administration. *Nanotoxicology* **2012**, *6*, 36−46.
(22) Hirn, S.; Semmler-Behnke, M.; Schleh, C.; Wenk, A.; Lipka, J.; Schaffler, M.; Takenaka, S.; Möller, W.; Schmid, G.; Simon, U.; Kreyling, W. G. Particle Size-Dependent and Surface Charge-Dependent Biodistribution of Gold Nanoparticles after Intravenous Administration. *Eur. J. Pharm. Biopharm.* **2011**, *77*, 407−416.
(23) Hume, D. A. Differentiation and Heterogeneity in the Mononuclear Phagocyte System. *Mucosal Immunol.* **2008**, *1*, 432−441.
(24) Almeida, J. P. M.; Chen, A. L.; Foster, A.; Drezek, R. *In Vivo* Biodistribution of Nanoparticles. *Nanomedicine (London, U. K.)* **2011**, *6*, 815−835.
(25) Zarschler, K.; Rocks, L.; Licciardello, N.; Boselli, L.; Polo, E.; Garcia, K. P.; De Cola, L.; Stephan, H.; Dawson, K. A. Ultrasmall Inorganic Nanoparticles: State-of-the-Art and Perspectives for Biomedical Applications. *Nanomedicine (N. Y., NY, U. S.)* **2016**, *12*, 1663−1701.
(26) Kreyling, W. G.; Holzwarth, U.; Haberl, N.; Kozempel, J.; Hirn, S.; Wenk, A.; Schleh, C.; Schäffler, M.; Lipka, J.; Semmler-Behnke, M.; Gibson, N. Quantitative Biokinetics of Titanium Dioxide Nanoparticles after Intravenous Injection in Rats: Part 1. *Nanotoxicology* **2017**, *11*, 434−442.
(27) Kreyling, W. G.; Holzwarth, U.; Haberl, N.; Kozempel, J.; Wenk, A.; Hirn, S.; Schleh, C.; Schäffler, M.; Lipka, J.; Semmler-Behnke, M.; Gibson, N. Quantitative Biokinetics of Titanium Dioxide Nanoparticles after Intratracheal Instillation in Rats: Part 3. *Nanotoxicology* **2017**, *11*, 454−464.
(28) Takenaka, S.; Karg, E.; Kreyling, W. G.; Lentner, B.; Möller, W.; Behnke-Semmler, M.; Jennen, L.; Walch, A.; Michalke, B.; Schramel, P.; Heyder, J.; Schulz, H. Distribution Pattern of Inhaled Ultrafine Gold Particles in the Rat Lung. *Inhalation Toxicol.* **2006**, *18*, 733−740.
(29) Takenaka, S.; Möller, W.; Semmler-Behnke, M.; Karg, E.; Wenk, A.; Schmid, O.; Stoeger, T.; Jennen, L.; Aichler, M.; Walch, A.; Pokhrel, S.; Madler, L.; Eickelberg, O.; Kreyling, W. G. Efficient Internalization and Intracellular Translocation of Inhaled Gold

DOI: 10.1021/acsnano.8b01826
ACS Nano 2018, 12, 7771−7790

Nanoparticles in Rat Alveolar Macrophages. *Nanomedicine (London, U. K.)* **2012**, *7*, 855−865.
(30) Geiser, M.; Quaile, O.; Wenk, A.; Wigge, C.; Eigeldinger-Berthou, S.; Hirn, S.; Schaffler, M.; Schleh, C.; Möller, W.; Mall, M. A.; Kreyling, W. G. Cellular Uptake and Localization of Inhaled Gold Nanoparticles in Lungs of Mice with Chronic Obstructive Pulmonary Disease. *Part. Fibre Toxicol.* **2013**, *10*, 19.
(31) Schleh, C.; Holzwarth, U.; Hirn, S.; Wenk, A.; Simonelli, F.; Schaffler, M.; Möller, W.; Gibson, N.; Kreyling, W. G. Biodistribution of Inhaled Gold Nanoparticles in Mice and the Influence of Surfactant Protein D. *J. Aerosol Med. Pulm. Drug Delivery* **2013**, *26*, 24−30.
(32) Tschanz, S. A.; Salm, L. A.; Roth-Kleiner, M.; Barré, S. F.; Burri, P. H.; Schittny, J. C. Rat Lungs Show a Biphasic Formation of New Alveoli During Postnatal Development. *J. Appl. Physiol.* **2014**, *117*, 89−95.
(33) Barré, S. F.; Haberthür, D.; Cremona, T. P.; Stampanoni, M.; Schittny, J. C. The Total Number of Acini Remains Constant Throughout Postnatal Rat Lung Development. *Am.J. Physiol.-Lung Cell. Mol. Physiol.* **2016**, *311*, L1082−L1089.
(34) Hofemeier, P.; Koshiyama, K.; Wada, S.; Sznitman, J. One (Sub-)Acinus for All: Fate of Inhaled Aerosols in Heterogeneous Pulmonary Acinar Structures. *Eur. J. Pharm. Sci.* **2018**, *113*, 53−63.
(35) Schittny, J. C.; Benner, C. F.; Cremona, T. P.; Haberthür, D.; Hasler, D.; Latzin, P.; Obrist, D. Computational Model of a Breathing Lung Illustrates the Influence of the Acinar Structures on Gas Washout. *Am. J. Respir. Crit. Care Med.* **2017**, *195*, A4440.
(36) Tschanz, S. A.; Salm, L. A.; Roth-Kleiner, M.; Barre, S. F.; Burri, P. H.; Schittny, J. C. Rat Lungs Show a Biphasic Formation of New Alveoli During Postnatal Development. *J. Appl. Physiol.* **2014**, *117*, 89−95.
(37) Hughes, J. M. B.; Amis, T. C., Regional Ventilation Distribution. In *Gas Mixing and Distribution in the Lung*; Engel, L. A., Paiva, M., Eds.; Marcel Dekker, Inc.: New York, 1985; pp 177−217.
(38) Brown, J. S., Deposition of Particles In *Comparative Biology of the Normal Lung*; Parent, R. A., Ed.; Academic Press−Elsevier: London, San Diego, 2015; pp 513−536.
(39) *Multiple-Path Particle Dosimetry Model (MPPD Version 3.0)*; ARA, 2009.
(40) Human Respiratory Tract Model for Radiological Protection. A Report of a Task Group of the International Commission on Radiological Protection. *Ann. ICRP* **1994**, *24*, 1−482, ICRP Publication 66.
(41) Oberdorster, G.; Ferin, J.; Morrow, P. E. Volumetric Loading of Alveolar Macrophages (Am): A Possible Basis for Diminished Am-Mediated Particle Clearance. *Exp. Lung Res.* **1992**, *18*, 87−104.
(42) Kreyling, W.; Scheuch, G., Clearance of Particles Deposited in the Lungs. In *Particle Lung Interactions*; Heyder, J., Gehr, P., Eds.; Marcel Dekker: New York, 2000; pp 323−376.
(43) Kreyling, W. G. Interspecies Comparison of Lung Clearance of ″Insoluble. *J. Aerosol Med.* **1990**, *3*, S93−S110.
(44) Lehnert, B. E. Pulmonary and Thoracic Macrophage Subpopulations and Clearance of Particles from the Lung. *Environ. Health Perspect.* **1992**, *97*, 17−46.
(45) Adamson, I. Y.; Bowden, D. H. Adaptive Responses of the Pulmonary Macrophagic System to Carbon. II. Morphologic Studies. *Lab. Invest.* **1978**, *38*, 430−438.
(46) Adamson, I. Y.; Bowden, D. H. Dose Response of the Pulmonary Macrophagic System to Various Particulates and Its Relationship to Transepithelial Passage of Free Particles. *Exp. Lung Res.* **1981**, *2*, 165−175.
(47) Bowden, D. H.; Adamson, I. Y. Pathways of Cellular Efflux and Particulate Clearance after Carbon Instillation to the Lung. *J. Pathol.* **1984**, *143*, 117−125.
(48) Thorley, A. J.; Ruenraroengsak, P.; Potter, T. E.; Tetley, T. D. Critical Determinants of Uptake and Translocation of Nanoparticles by the Human Pulmonary Alveolar Epithelium. *ACS Nano* **2014**, *8*, 11778−11789.
(49) Geiser, M.; Rothen-Rutishauser, B.; Kapp, N.; Schurch, S.; Kreyling, W.; Schulz, H.; Semmler, M.; Im Hof, V.; Heyder, J.; Gehr, P. Ultrafine Particles Cross Cellular Membranes by Nonphagocytic Mechanisms in Lungs and in Cultured Cells. Environ. *Health Perspect* **2005**, *113*, 1555−1560.
(50) Nunn, J. F. Functional Anatomy of the Respiratory Tract. In *Nunn's Applied Respiratory Physiology* 4th ed.; Butterworth-Heinemann, 1993; Chapter 2, pp 13−35.
(51) Weibel, E. R. On the Tricks Alveolar Epithelial Cells Play to Make a Good Lung. *Am. J. Respir. Crit. Care Med.* **2015**, *191*, 504−513.
(52) Macklin, C. C. Pulmonary Sumps, Dust Accumulations, Alveolar Fluid and Lymph Vessels. *Cells Tissues Organs* **2004**, *23*, 1−33.
(53) Oberdörster, G.; Oberdörster, E.; Oberdörster, J. Nanotoxicology: An Emerging Discipline Evolving from Studies of Ultrafine Particles. *Environ. Health Perspect* **2005**, *113*, 823−839.
(54) Plesch, B. E. Histology and Immunohistochemistry of Bronchus Associated Lymphoid Tissue (Balt) in the Rat. *Adv. Exp. Med. Biol.* **1982**, *149*, 491−497.
(55) Fromen, C. A.; Rahhal, T. B.; Robbins, G. R.; Kai, M. P.; Shen, T. W.; Luft, J. C.; DeSimone, J. M. Nanoparticle Surface Charge Impacts Distribution, Uptake and Lymph Node Trafficking by Pulmonary Antigen-Presenting Cells. *Nanomedicine (N. Y., NY, U. S.)* **2016**, *12*, 677−687.
(56) Roth, C.; Scheuch, G.; Stahlhofen, W. Proceedings of the 1993 European Aerosol Conference 14 O 04 Clearance of the Human Lungs for Ultrafine Particles. *J. Aerosol Sci.* **1993**, *24*, S95−S96.
(57) Wagner, P. E.; Kreyling, W. G.; Semmler, M.; Müller, W. Health Effects of Ultrafine Particles. *J. Aerosol Sci.* **2004**, *35*, 1155−1156.
(58) Möller, W.; Barth, W.; Kohlhaufl, M.; Haussinger, K.; Stahlhofen, W.; Heyder, J. Human Alveolar Long-Term Clearance of Ferromagnetic Iron Oxide Microparticles in Healthy and Diseased Subjects. *Exp. Lung Res.* **2001**, *27*, 547−568.
(59) Möller, W.; Felten, K.; Sommerer, K.; Scheuch, G.; Meyer, G.; Meyer, P.; Haussinger, K.; Kreyling, W. G. Deposition, Retention, and Translocation of Ultrafine Particles from the Central Airways and Lung Periphery. *Am. J. Respir. Crit. Care Med.* **2008**, *177*, 426−432.
(60) Snipes, M. B.; Boecker, B. B.; McClellan, R. O. Retention of Monodisperse or Polydisperse Aluminosilicate Particles Inhaled by Dogs, Rats, and Mice. *Toxicol. Appl. Pharmacol.* **1983**, *69*, 345−362.
(61) Pan, Y.; Leifert, A.; Ruau, D.; Neuss, S.; Bornemann, J.; Schmid, G.; Brandau, W.; Simon, U.; Jahnen-Dechent, W. Gold Nanoparticles of Diameter 1.4 Nm Trigger Necrosis by Oxidative Stress and Mitochondrial Damage. *Small* **2009**, *5*, 2067−2076.
(62) Pan, Y.; Neuss, S.; Leifert, A.; Fischler, M.; Wen, F.; Simon, U.; Schmid, G.; Brandau, W.; Jahnen-Dechent, W. Size-Dependent Cytotoxicity of Gold Nanoparticles. *Small* **2007**, *3*, 1941−1949.
(63) Tsoli, M.; Kuhn, H.; Brandau, W.; Esche, H.; Schmid, G. Cellular Uptake and Toxicity of Au55 Clusters. *Small* **2005**, *1*, 841−844.
(64) Kreyling, W. G.; Holzwarth, U.; Schleh, C.; Kozempel, J.; Wenk, A.; Haberl, N.; Hirn, S.; Schäffler, M.; Lipka, J.; Semmler-Behnke, M.; Gibson, N. Quantitative Biokinetics of Titanium Dioxide Nanoparticles after Oral Application in Rats: Part 2. *Nanotoxicology* **2017**, *11*, 443−453.
(65) Hainfeld, J. F.; Slatkin, D. N.; Focella, T. M.; Smilowitz, H. M. Gold Nanoparticles: A New X-Ray Contrast Agent. *Br. J. Radiol.* **2006**, *79*, 248−253.
(66) Hainfeld, J. F.; Slatkin, D. N.; Smilowitz, H. M. The Use of Gold Nanoparticles to Enhance Radiotherapy in Mice. *Phys. Med. Biol.* **2004**, *49*, N309−N315.
(67) Choi, H. S.; Liu, W.; Misra, P.; Tanaka, E.; Zimmer, J. P.; Ipe, B. I.; Bawendi, M. G.; Frangioni, J. V. Renal Clearance of Quantum Dots. *Nat. Biotechnol.* **2007**, *25*, 1165−1170.
(68) Alric, C.; Miladi, I.; Kryza, D.; Taleb, J.; Lux, F.; Bazzi, R.; Billotey, C.; Janier, M.; Perriat, P.; Roux, S.; Tillement, O. The

DOI: 10.1021/acsnano.8b01826
ACS Nano 2018, 12, 7771−7790

Biodistribution of Gold Nanoparticles Designed for Renal Clearance. *Nanoscale* **2013**, *5*, 5930−5939.
(69) Chen, F.; Goel, S.; Hernandez, R.; Graves, S. A.; Shi, S.; Nickles, R. J.; Cai, W. Dynamic Positron Emission Tomography Imaging of Renal Clearable Gold Nanoparticles. *Small* **2016**, *12*, 2775−2782.
(70) Miller, M. R.; Raftis, J. B.; Langrish, J. P.; McLean, S. G.; Samutrtai, P.; Connell, S. P.; Wilson, S.; Vesey, A. T.; Fokkens, P. H. B.; Boere, A. J. F.; Krystek, P.; Campbell, C. J.; Hadoke, P. W. F.; Donaldson, K.; Cassee, F. R.; Newby, D. E.; Duffin, R.; Mills, N. L. Correction to″Inhaled Nanoparticles Accumulate at Sites of Vascular Disease″. *ACS Nano* **2017**, *11*, 10623−10624.
(71) Möller, W.; Gibson, N.; Geiser, M.; Pokhrel, S.; Wenk, A.; Takenaka, S.; Schmid, O.; Bulgheroni, A.; Simonelli, F.; Kozempel, J.; Holzwarth, U.; Wigge, C.; Eigeldinger-Berthou, S.; Mädler, L.; Kreyling, W. Gold Nanoparticle Aerosols for Rodent Inhalation and Translocation Studies. *J. Nanopart. Res.* **2013**, *15*, 1574.
(72) Ditroi, F.; Tarkanyi, F.; Takacs, S.; Hermanne, A. Activation Cross Sections of Proton Induced Nuclear Reactions on Gold up to 65 Mev. *Appl. Radiat. Isot.* **2016**, *113*, 96−109.
(73) Alessandrini, F.; Semmler-Behnke, M.; Jakob, T.; Schulz, H.; Behrendt, H.; Kreyling, W. Total and Regional Deposition of Ultrafine Particles in a Mouse Model of Allergic Inflammation of the Lung. *Inhalation Toxicol.* **2008**, *20*, 585−593.
(74) Kreyling, W. G.; Semmler-Behnke, M.; Seitz, J.; Scymczak, W.; Wenk, A.; Mayer, P.; Takenaka, S.; Oberdorster, G. Size Dependence of the Translocation of Inhaled Iridium and Carbon Nanoparticle Aggregates from the Lung of Rats to the Blood and Secondary Target Organs. *Inhalation Toxicol.* **2009**, *21*, 55−60.
(75) Kreyling, W. G. Discovery of Unique and Enm— Specific Pathophysiologic Pathways: Comparison of the Translocation of Inhaled Iridium Nanoparticles from Nasal Epithelium *Versus* Alveolar Epithelium Towards the Brain of Rats. *Toxicol. Appl. Pharmacol.* **2016**, *299*, 41−46.
(76) Haberthür, D.; Semmler-Behnke, M.; Takenaka, S.; Kreyling, W. G.; Stampanoni, M.; Tsuda, A.; Schittny, J. C. Multimodal Imaging for the Detection of Sub-Micron Particles in the Gas-Exchange Region of the Mammalian Lung. *J. Phys.: Conf. Ser.* **2009**, *186*, 012040.
(77) Sweeney, T. D.; Brain, J. D.; Leavitt, S. A.; Godleski, J. J. Emphysema Alters the Deposition Pattern of Inhaled Particles in Hamsters. *Am. J. Physiol.* **1987**, *128*, 19−28.
(78) Valberg, P. A.; Brain, J. D.; Sneddon, S. L.; LeMott, S. R. Breathing Patterns Influence Aerosol Deposition Sites in Excised Dog Lungs. *J. Appl. Physiol.* **1982**, *53*, 824−837.
(79) Schindelin, J.; Arganda-Carreras, I.; Frise, E.; Kaynig, V.; Longair, M.; Pietzsch, T.; Preibisch, S.; Rueden, C.; Saalfeld, S.; Schmid, B.; Tinevez, J.-Y.; White, D.; Hartenstein, V.; Eliceiri, K.; Tomancak, P.; Cardona, A. Fiji: An Open-Source Platform for Biological-Image Analysis. *Nat. Methods* **2012**, *9*, 676−682.
(80) Oeff, K.; Konig, A. [Blood Volume of Rat Organs and Residual Amount of Blood after Blood Letting or Irrigation; Determination with Radiophosphorus-Labeled Erythrocytes.]. *Naunyn-Schmiedeberg's Arch. Pharmacol.* **1955**, *226*, 98−102.
(81) Kreyling, W. G.; Hirn, S.; Möller, W.; Schleh, C.; Wenk, A.; Celik, G.; Lipka, J.; Schäffler, M.; Haberl, N.; Johnston, B. D.; Sperling, R.; Schmid, G.; Simon, U.; Parak, W. J.; Semmler-Behnke, M. Air−Blood Barrier Translocation of Tracheally Instilled Gold Nanoparticles Inversely Depends on Particle Size. *ACS Nano* **2014**, *8*, 222−223.

DOI: 10.1021/acsnano.8b01826
ACS Nano 2018, 12, 7771−7790